Table of Contents

List of Tables

Annual CO dark production in global coastal waters (water depth <200m).

List of Figures

List of Abbreviations and Symbols

Symbol	Definition	Units
$\Phi_{co}(\lambda)$	Apparent quantum yield of CO	mol CO (mol photons)$^{-1}$
$\overline{\Phi}_{co}$	Solar insolation-weighted mean apparent quantum yield of CO	mol CO (mol photons)$^{-1}$
β_{co}	[CDOM]-normalized CO dark production rate, i.e., Q_{co}/a_{350})	nmol L^{-1} h^{-1} m
Λ	wavelength	nm
A	Cross section of quartz cell	m^2
A(λ)	Absorbance at wavelength λ	
$A(\lambda)$	Absorption coefficient at wavelength λ	m^{-1}
CDOM	Chromophoric dissolved organic matter	
AQY	Apparent quantum yield	
chl-a	Chlorophyll-a	
CO	Carbon monoxide	
CO_2	Carbon dioxide	
DIC	Dissolved inorganic carbon	
DOC	Dissolved organic carbon	
DOM	Dissolved organic matter	
E_a	Activation energy	J mol^{-1}
F_{330}	Fraction of the original a_{330}	
Gg	Gigagrams (10^9grams)	
GSL	Gulf of St. Lawrence	
$Q_{in}(\lambda)$	incident irradiance	mol photons m^{-2} s^{-1} nm^{-1}
L	Pathlength of light	m
LSLE	Lower St. Lawrence estuary	
P_i	Measured CO production rate in the ith irradiation cell	mol m^{-3} s^{-1}
$<P_i>$	Predicted CO production rate in the ith irradiation cell	mol m^{-3} s^{-1}
PAP	Pointe- au-Pére	
Q(λ)	Photon flux at wavelength λ	moles photons m^{-2} s^{-1} nm^{-1}
Q_{co}	Dark production rate of CO	nmol L^{-1} h^{-1}
RR	Rimouski River	
S	Salinity	psu
SF	Saguenay Fjord	
SLES	St. Lawrence estuarine system	
$SUVA_{254}$	Specific absorption coefficient at 254nm	L (mg C)$^{-1}$ m^{-1}
T	Temperature	Kelvin
Tg	Teragram(10^{12}gram)	
USLE	Upper St. Lawrence Estuary	
UV-A	Ultraviolet radiation between 280-320nm	
UV-B	Ultraviolet radiation between 320-400nm	
µm	micrometer	

Acknowledgments

I thank all the members of my committee for their advice, support and criticism generously provided throughout this work. I am particularly indebted to Huixiang Xie for identification of a rewarding field of study, and for his encouragement and many enlightening discussions. Many thanks are extended to S. Bélanger and R. Villeneuve for measuring CDOM absorbance; A. Rochon for assistance in sample collection; J. Caveen for Matlab programming; G. Canuel for analyzing salinity samples; C. Aubry for technical assistance; the scientists, colleagues, and the captains and crew of the *Coriolis II* cruises for their cooperation during the field investigations.

This work was supported by grants from the Natural Sciences and Engineering Research Council of Canada (NSERC) and the Canada Foundation for Innovation (CFI). Y. Zhang was supported by a Quebec-China Merit Fellowship and an ISMER graduate fellowship.

Chapter 1. Introduction

1.1. Significance of CO study

The ocean is a net source of atmospheric carbon monoxide (CO) (Swinnerton et al., 1970; Bates et al., 1995), which regulates the oxidizing capacity of the atmosphere (Derwent, 1995) and acts as an indirect green-house-effect gas that is partly responsible for global warming (Zepp et al., 1998). CO in the surface ocean is produced primarily from the photolysis of chromophoric dissolved organic matter (CDOM) (Conrad et al., 1982; Zafiriou et al., 2003) and is lost by microbial consumption and outgassing (Conrad et al., 1982; Johnson and Bates, 1996; Zafiriou et al., 2003; Xie et al., 2005). Limited data also show that thermal degradation of DOM (Xie et al., 2005). and certain marine organisms (King, 2001) also produce CO.

Current estimates of the dissolved organic carbon sink associated with DOM photodegradation are 10-30% of total oceanic primary production (Miller and Moran, 1997; Mopper and Kierber, 2000), and are hence clearly relevant on global scales. CO is quantitatively the second largest identified inorganic carbon product of marine DOM photolysis (Mopper and Kierber, 2000). Therefore, CO photoproduction is, by itself, of biogeochemical significance. CO is also considered a useful proxy for general CDOM photoreactivity and for the difficult–to–measure photoproduction of dissolved inorganic carbon (Miller and Zepp, 1995; Johannessen, 2000; Mopper and Kierber, 2000) and biolabile carbon (Kieber et al., 1989; Moran and Zepp, 1997; Miller et al., 2002), which together have been proposed to be one of the major terms in the ocean carbon cycle. Moreover, CO has emerged as a key tracer for use in testing and tuning models of various

mixed-layer processes, including photochemistry, ocean optics, radiative flux, mixing and air-sea gas exchange (Kettle, 1994; Doney et al., 1995; Najjar et al., 1995; Gnanadesikan, 1996; Johnson and Bates, 1996; 2005). Finally, CO acts as a supplemental energy source to some lithoheterotrophs, which mediate a major fraction of CO oxidation in ocean surface water (Moran and Miller, 2007). Therefore, any significant advances or modifications in our knowledge of oceanic CO would affect our view of other major marine biogeochemical cycles.

1.2. Existing problems in CO research

Open-ocean CO photoproduction is reasonably constrained (30-90 Tg CO-C a^{-1}) (Zafiriou et al., 2003; Stubbins et al., 2006a). However, spatial and seasonal variability in the levels, sources and nature of the photoreactant, CDOM, in rivers, estuaries, and terrestrially and upwelling-influenced seas, make photoproduction rates for these aquatic environments hard to predict and, therefore, rates are poorly constrained (Valentine and Zepp, 1993; Zuo and Jones, 1995; Law et al., 2002; Zhang et al., 2006). Estimates of the total marine photoproduction have not advanced in recent years, ranging from 30 to 820 Tg CO-C a^{-1} (Valentine and Zepp, 1993; Zuo and Jones, 1995; Moran and Zepp, 1997) and only a tentative estimate of global estuarine CO photoproduction exists (~2 Tg CO-C a^{-1}) (Stubbins, 2001). The significance of CO photoproduction and the uncertainty in current estimates are best illustrated by comparison with other carbon cycle terms. For example, estimates of the total marine photochemical CO source are equivalent to 8-200% of global riverine DOM inputs (Prather et al., 2001) and 16-350% of carbon burial

in marine sediments (Hedges et al., 1997). These comparisons clearly illustrate the importance of CO photoproduction and the requirement to better constrain its potential contribution to aquatic carbon cycling.

To quantitatively assess the role of CDOM photooxidation in the fate of organic carbon in the ocean (Miller and Zepp, 1995; Andrews et al., 2000; Vahatalo and Wetzel, 2004), two approaches have been employed most frequently: in situ incubations (Kieber et al., 1997) and optical-photochemical coupled modeling based on apparent quantum yields (AQYs) (Valentine and Zepp, 1993; Johannessen, 2000; Bélanger et al., 2006). The former determines water column photochemical fluxes by directly incubating water samples at varying depths in the photic zone; it requires laborious fieldwork, but is thought to closely simulate the natural photochemistry and the in situ light field. The latter calculates photochemical rates by combining experimentally determined AQY spectra with CDOM absorption coefficient spectra and underwater irradiance. As CDOM absorption coefficients can be retrieved from satellite ocean color measurements (Siegel et al., 2002; Bélanger et al., 2008; Fichot et al., 2008), the modeling approach appears promising for large-scale investigations (Johannessen, 2000; Miller and Fichot, 2006). The reliability of this approach depends, to a large extent, on the reliability of the AQY spectra used in the model. Potentially large uncertainties in published AQY spectra are partly associated with the lack of quantitative knowledge of the influences of CDOM quality and environmental conditions on the related photoprocesses, including CO photoproduction.

Thermal (dark) production of CO, another potentially important marine CO source, has so far drawn little attention and its regional and global-scale source strengths

are unknown. (Xie et al., 2005) observed CO dark formation rates of 0.21 ± 0.21 nmol L^{-1} h^{-1} in nine cyanide-poisoned Delaware Bay water samples. Significant CO dark production was also inferred from modeling upper-ocean CO cycles (Kettle, 1994, 2005). The dark production term is often critical to rationalize model–data discrepancies and greatly affects the values of CO photoproduction and microbial uptake rates that are derived from inverse modeling approaches (Kettle, 2005). Therefore, the lack of quantitative knowledge of this pathway seriously limits modeling and may add substantial uncertainties to the global marine CO budget.

It is expected that the distribution and biogeochemical cycling of CO in coastal (including estuarine) waters would be different from those in the open ocean due at least to 1) coastal waters are highly enriched with DOM relative to blue waters, causing the photochemical depth scale (e.g., e-folding depth of light at 320 nm) in coastal waters to be smaller than that in the open ocean; 2) coastal DOM is largely of terrestrial origin while DOM in remote-ocean areas is dominantly of marine origin, which could result in different efficiencies of CO production; 3) the far more complex hydrological, physical, chemical and biological dynamics in coastal zones should give rise to more complicated influences on CO cycling in these areas.

1.3. Objectives

The overall goal of this project aims at improving the estimates of CO source strengths by investigating the CO photo and dark productions in a high mid-latitude estuarine system–the St. Lawrence estuarine system (SLES). This goal will be

accomplished through the following specific objectives:

1) To determine the spatial variability of the apparent quantum yield spectrum of CO photoproduction (Φ_{co}) and evaluate the effects of water temperature, CDOM's origin and light history on Φ_{co}.

2) To determine the spatial variability of the CO dark production (Q_{co}) and assess the effects of temperature, salinity, pH, and CDOM abundance and origin on Q_{co}.

3) To establish empirical, predictive relationships between Φ_{co} (and Q_{co}) and relevant environmental variables, such as CDOM absorption, water temperature, pH, and salinity.

4) To model the annual CO photo and dark productions in SLES based on the empirical equations.

5) To provide an estimate of global-scale CO dark production fluxes by extrapolation.

Chapter 2. Methods

2.1. Study area

The estuary and Gulf of St. Lawrence, referred to as the St. Lawrence estuarine system (SLES) herein, is a semi-enclosed water body with connections to the Atlantic Ocean through the Cabot and Belle-Isle strait (Figure.2-1). It receives the second largest freshwater discharge (600 km^3 a^{-1}) in North America (Koutitonsky and Bugden 1991; Strain, 1990). Over a relatively small horizontal scale (~1200 km), the SLES provides various hydrological, geographical and oceanographic features. Surface water in the SLES transitions from freshwater-dominated CASE 2 water in the estuary to oceanic water-dominated CASE 1 water in the Gulf (Nieke et al., 1997). The water column is fairly well mixed in the upper estuary (Quebec City to the mouth of the Saguenay Fjord) but highly stratified, except in winter, in the lower estuary (the mouth of Saguenay Fjord to Pointe-des-Monts) and the Gulf. An average depth of ~60 m in the upper estuary drops abruptly to >200 m over a few kilometers near the mouth of the Saguenay Fjord (Dickie and Trites, 1983). The typical two-layer estuarine circulation creates a maximum turbidity zone near Île d'Orléans, slightly downstream of Quebec City (d'Anglejan and Smith, 1973). Among the other facets of the SLES are runoff plumes, gyres, fronts, and upwelling areas (Koutitonsky and Bugden, 1991). These features make the SLES an ideal natural laboratory to study the transition of biogeochemical processes from freshwater to estuarine to oceanic water systems.

2.2. Method for CO photoproduction

2.2.1. Sample collection and treatment.

Sampling stations were dispersed along a salinity gradient from the upstream limit of the St. Lawrence estuary near Quebec City through the Gulf of St. Lawrence and to the open Atlantic off Cabot Strait. Thirteen stations (Stns. 1-13) were sampled for absorbance and DOC measurements and six (Stns. 1, 3, 8, 11, 12, 13) for the AQY study (Figure 2-1).Water samples (2 m deep) were taken in late July 2004 for Stns. 1-12 and in mid-June 2005 for Stn. 13 using 12-L Niskin bottles attached to a CTD rosette. Samples were gravity-filtered upon collection through Pall AcroPak 1000 capsules sequentially containing 0.8 μm and 0.2 μm polyethersulfone membrane filters. The filtered water was transferred in darkness into acid-cleaned, 4 L clear glass bottles, stored in darkness at 4 ^{o}C, and brought back to the laboratory at Rimouski. Samples were re-filtered with 0.22 μm polycarbonate membranes (Millipore) and purged with CO-free air immediately prior to irradiations, which were carried out within 2 months of sample collection.

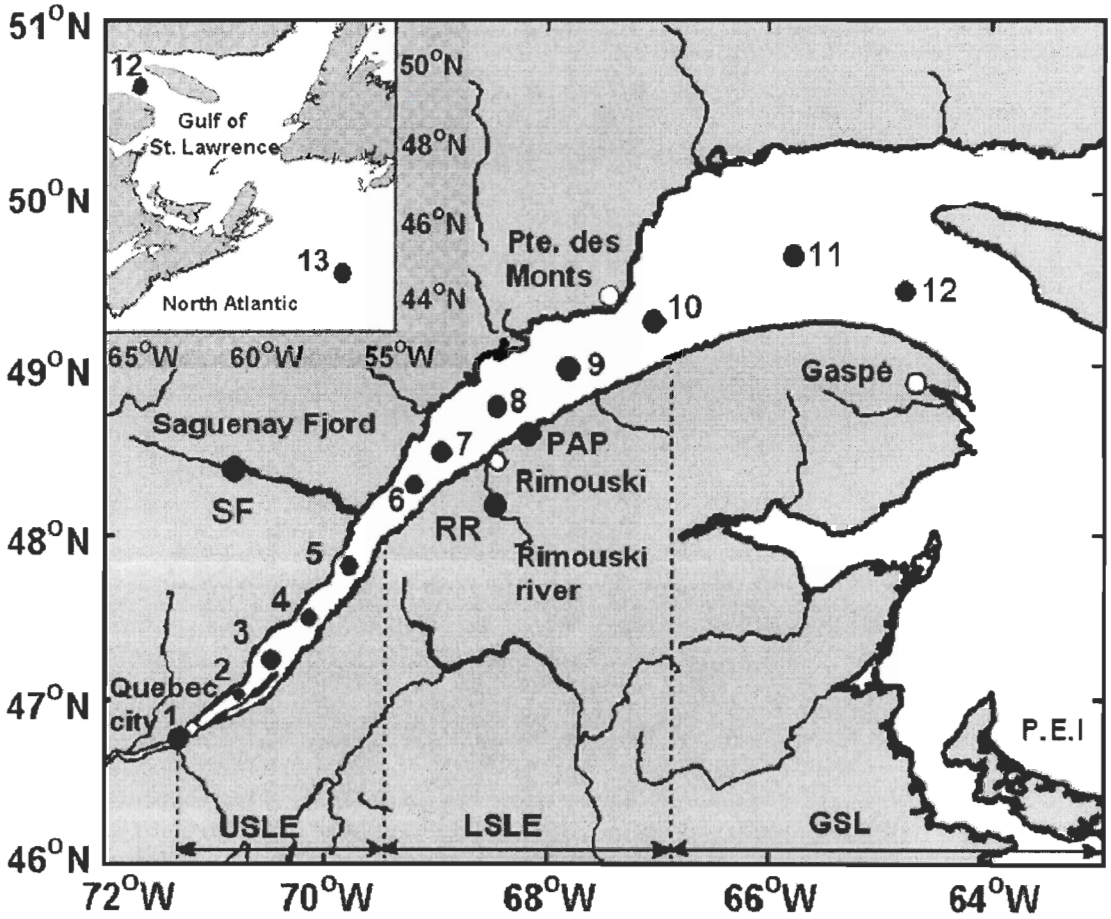

Figure 2-1. Sampling locations in the St. Lawrence estuarine system and in the Atlantic Ocean off the Cabot Strait.

2.2.2. Photobleaching

In order to evaluate the effect of the CDOM's light history on Φ_{co} (i.e., dose dependence), filtered samples, placed in a clear glass container covered with a quartz plate, kept at 15 °C and continuously stirred, were irradiated with a SUNTEST XLS+ solar simulator equipped with a 1.5KW xenon lamp. Radiations emitted from the xenon lamp were screened by a Suprax long band-pass cutoff filter to minimize radiations <290 nm, and the spectral composition of the solar simulator closely matched that of natural sunlight reaching the earth's surface. The output of the lamp was adjusted to 765 W m^{-2} (280-800nm) at the irradiation surface as determined with an OL-754 UV-vis spectroradiometer (Optronics Laboratories) fitted with an OL IS-270 2 in. integrating sphere. Irradiation time varied from 20 min to 175.0 h to obtain various photobleaching regimes.

2.2.3. Irradiation for Φ_{co} determination.

The irradiation setup (Figure 2-2) and procedure for determining Φ_{co} spectra were modified from Ziolkowski (2000). Briefly, water samples were purged with CO-free air (medical grade) to reduce the background CO concentration. At the end of purging, they were siphoned through a Teflon tube into pre-combusted (420°C) gas-tight quartz-windowed cylindrical cells (I.D.: 3.4 cm, length: 11.4 cm). The cells were rinsed with the sample water three times and overflowed three times the cell's volume prior to the final filling (without leaving headspace). Then the sample water in quartz cells were irradiated in a temperature-controlled incubator using a SUNTEST CPS solar simulator equipped

with a 1-kW xenon lamp. Except the top 2-mm sections, the cells were directly in contact with the cooling solution (a mixture of water and ethylene glycol). The outer sides of the quartz cells were wrapped in black electrical tape to prevent lateral leakage of radiation between cells. Eight spectral treatments were examined employing successive Schott long band-pass glass filters; their models are (numbers are nominal 50% transmission cutoff wavelength): WG280, WG295, WG305, WG320, WG345, GG395, GG435, and GG495). Spectral irradiance under each filter was measured, both before and after sample irradiation, using the OL-754 spectroradiometer fitted with a 2-inch OL IS-270 integrating sphere. The difference between the two measurements generally was within 1%.

Irradiation time varied from 10 min to 20.0 h, depending on the sample's CDOM concentration and the filter's cutoff wavelength. The irradiation time was chosen so that detectable amounts of CO were produced but minimum absorbance losses (<4% at 350 nm) were incurred. When significant absorbance losses occurred (3 out of total 456 occasions), the absorbance before and after irradiation were averaged for the calculation of Φ_{CO} according to first-order kinetic decay, which well describes CDOM photobleaching (Del Vecchio and Blough, 2002; Xie et al., 2004). To assess the effect of temperature on CO photoproduction, the original samples were irradiated at five temperatures: 0.5, 7.0, 15.0, 24.0, and 32.0°C. Reported irradiation temperatures were post-irradiation temperatures inside the cells. The dose dependence was evaluated only at 15°C. Thermal CO production in the parallel dark incubations was on average (± s.d.) 0.33% (± 0.36%) and 42% (± 21%) of the production under the WG280 and GG495 filter, respectively. Dark control values were subtracted as blanks.

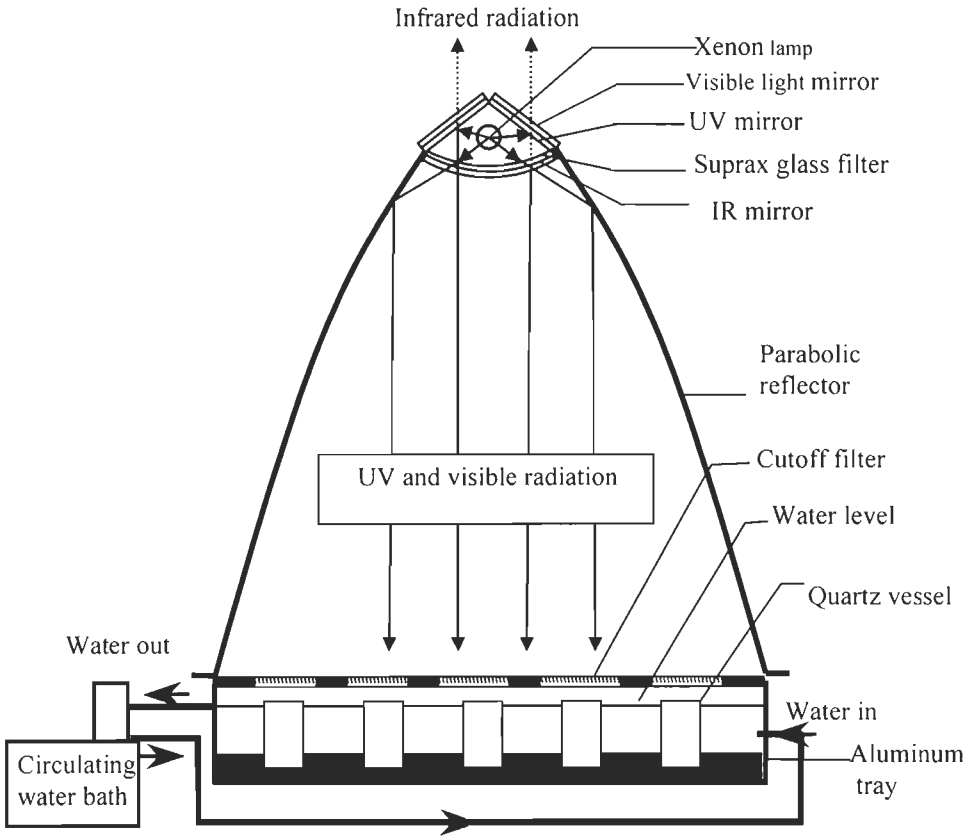

Figure 2-2: Cross section of the irradiation system

2.2.4. Calculation of Φ_{co}.

The spectral CO apparent quantum yield, $\Phi_{co}(\lambda)$, is defined as the number of moles of CO photochemically produced per mole of photons absorbed by CDOM at wavelength λ. A Matlab-coded iterative curve fit method (Ziolkowski, 2000; Johannessen and Miller, 2001) was employed to derive $\Phi_{co}(\lambda)$. Briefly, this method assumes an appropriate mathematical form with unknown parameters to express the change in Φ_{co} as a function of wavelength. Decreasing exponential functions are usually chosen for AQY spectra of CDOM photoprocesses (Vahatalo et al., 2000; Ziolkowski, 2000; Johannessen and Miller, 2001). The amount of CO produced in an irradiation cell over the exposure time can then be predicted as the product of the assumed $\Phi_{co}(\lambda)$ function and the number of photons absorbed by CDOM integrated over the 250-600 nm wavelength range, assuming no CO photoproduction above 600 nm. We followed Hu et al.'s (2002) recommendations to calculate the number of photons absorbed by CDOM at a specific wavelength λ ($Q_{CDOM}(\lambda)$):

$$Q_{CDOM}(\lambda) = \frac{a_{CDOM}(\lambda)}{a_t(\lambda)} \times Q_{in}(\lambda) \times [1 - \exp(-a_t(\lambda) \times L)] \text{ (mol photons } m^{-2}\ s^{-1}\ nm^{-1}) \text{.....(2-1)}$$

where L is the pathlength of the cells, $Q_{in}(\lambda)$ is the incident irradiance just below the upper window of the cells (Figure 2-3), $a_t(\lambda)$ is the total absorption coefficient, which is the sum of the absorption by CDOM ($a_{CDOM}(\lambda)$) and water ($a_w(\lambda)$) (no absorption by particles since our samples were 0.2-μm filtered). The absorption coefficients of water were taken from Pope and Fry (1997) and Buiteveld et al. (1994).

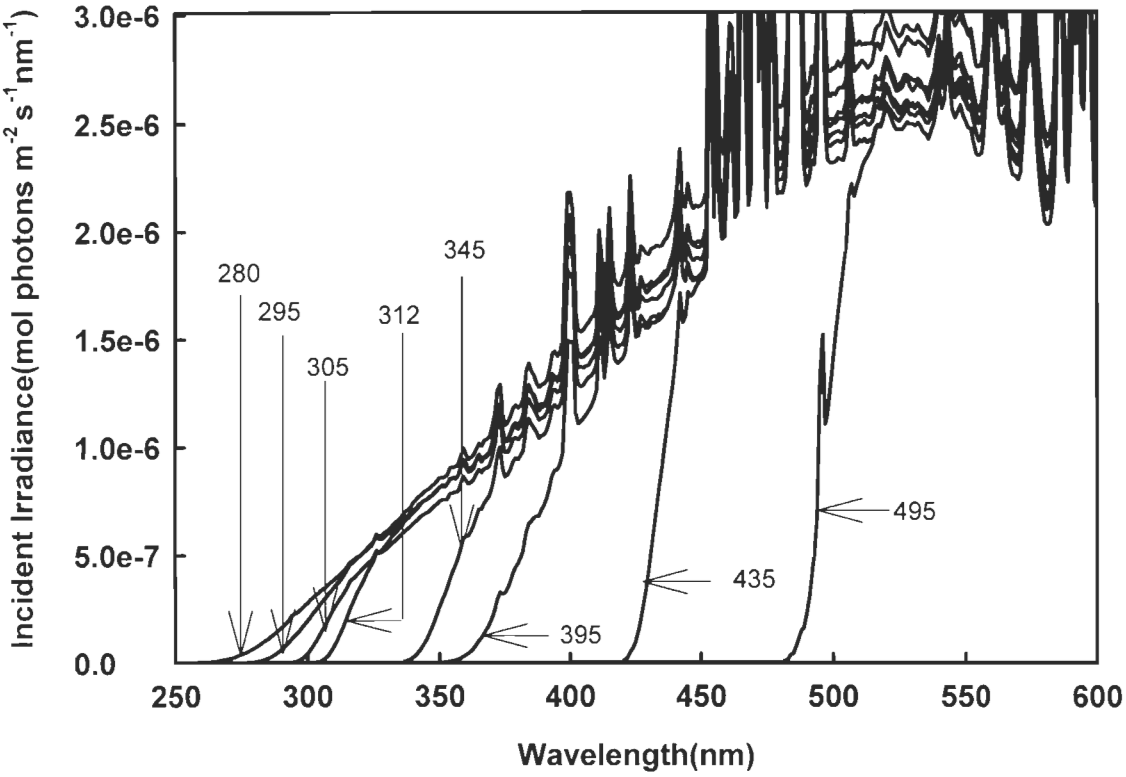

Figure 2-3. Incident irradiance in each quartz cell. Numbers at the end of arrows stand for the models of the Shott cutoff filters.

Using the assumed mathematical form of Φ_{co} (λ) , we can predict the CO production rate in the i^{th} irradiation cell, $<P_i>$, to be

$$< P_i >= L^{-1} \int_{\lambda} \Phi_{co}(\lambda) Q_{CDOM}(\lambda) d\lambda \ \text{(moles m}^{-3}\ \text{s}^{-1}) \tag{2-2}$$

The χ^2 error between the measured CO production rate (P_i) in the i^{th} irradiation cell and the corresponding predicted one ($<P_i>$) can be calculated as:

$$\chi^2 = \sum_{i=1}^{8} [log(\langle P_i \rangle) - log(P_i)]^2 \tag{2-3}$$

The optimum values of the unknown parameters in the assumed $\Phi_{co}(\lambda)$ function are obtained by varying these parameters from initial estimates until the χ^2 error was minimized.

The following quasi-exponential form was adopted to describe the relationship between Φ_{co} and λ:

$$\Phi_{co}(\lambda) = m_1 * \exp\left(\frac{m_2}{\lambda + m_3}\right) \tag{2-4}$$

where m_1, m_2, and m_3 are fitting parameters. This function has been demonstrated to perform generally better (Xie and Gosselin, 2005; Bélanger et al., 2006), particularly in the UV-A and visible wavelengths, than the more frequently used single exponential form.

To facilitate analysis of local Φ_{co} variability, we defined a solar spectrum weighted mean CO quantum yield (Bélanger et al., 2006), $\overline{\Phi}_{co}$, over the 280-600 nm range:

$$\overline{\Phi}_{co} = \frac{\int_{280}^{600} Q(\lambda)\Phi_{co}(\lambda)d\lambda}{\int_{280}^{600} Q(\lambda)d\lambda} \quad (2\text{-}5)$$

where $Q(\lambda)$ is the noontime cloudless spectral solar photon flux recorded at Rimouski (48.453°N, 68.511°W), Quebec, on 24 May 2005 (Table A1). The rationale for this normalization is to reduce the Φ_{co} spectrum to a single value that accounts for both the magnitudes and shapes of the Φ_{co} (λ) and $Q(\lambda)$ spectra, thereby giving more weight to the wavelengths at which CO production is maximum (i.e., 320-340 nm). From an environmental relevance perspective, $\overline{\Phi}_{co}$ corresponds to the solar insolation-normalized CO production in the water column in which all solar radiation over 280-600 nm is absorbed by CDOM. Note that the $\overline{\Phi}_{co}$ values presented here are specific to this study since they more or less depend on the specific $Q(\lambda)$ spectrum used.

2.3. Methods for CO dark production

2.3.1. Sampling

Sampling was conducted aboard the research ship *Coriolis II* between 3-9 May 2007. Four stations (Stns. 1, 3, 4, and 12) were distributed along an axial transect from the upstream limit of the estuary near Quebec City to the Gulf (Fig. 2-1). The same cruise also visited a site in the Saguenay Fjord (Stn SF in Fig. 2-1), an important tributary of the

SLES with its surface water being highly enriched with CDOM. Water samples were taken using 12-L Niskin bottles attached to a CTD rosette. They were gravity-filtered using sterile Pall AcroPak 500 capsules sequentially containing 0.8-μm and 0.2-μm polyethersulfone membrane filters. The capsules were connected to the Niskin bottles' spigot with clean silicon tubing. Prior to sample collection, the capsules were thoroughly rinsed with Nanopure water to avoid potential contamination. The filtered samples were transferred into acid-cleaned 4-L clear-glass bottles or 20-L collapsible polyethylene bags (Cole-Parmer) that were protected against sunlight. Samples in the glass bottles were used immediately upon collection for shipboard incubations. Because of the short duration of the cruise and the constraint on technical resources, those samples in the plastic bags had to be stored in darkness at 4°C and brought back to the laboratory at Rimouski for land-based incubations. Sampling depths for each station visited, along with other related parameters, are shown in Table 4-1.

2.3.2. Contamination assessment

Biological-oxygen-demand (BOD) bottles (300 mL) were used as incubating vessels. Prior to incubations, the BOD bottles were soaked in 10% HCl for over 24 h and rinsed thoroughly with Nanopure water. They were then filled with 0.2 μm-filtered, CO-depleted Nanopure water and incubated in the dark at room temperatures (~23 °C) for 96 h to check for potential contamination by bottles and filters. The CO formation rates in the bottles ranged -6.4×10^{-5} - 6.8×10^{-5} nmol L^{-1} h^{-1}, averaged 2.3×10^{-5} nmol L^{-1} h^{-1} ($\pm$ 6.0×10^{-5} nmol L^{-1} h^{-1}, n = 65), which are negligible compared to the detectable CO production rates in this study.

A surface (bucket) water sample was collected from the highly colored Rimouski River (Stn. RR in Fig. 2-1) to verify whether sample filtration could cause loss of DOM and thus reduce CO dark production. Part of the sample was filtered (0.2 μm) once while the remaining part was filtered twice. The twice-filtered water was incubated in parallel with the single-time filtered water. The two treatments gave essentially identical production values (<0.1%), proving no significant negative artifacts from filtration.

2.3.3. Shipboard incubations

Shipboard incubations were conducted to measure CO dark production rates, Q_{co}, at *in situ* temperatures and *pH* at Stns. 1, 4, 12 and SF. Each sample was purged in the dark with CO-free air (medical grade) to minimize background CO concentration ([CO]), and then siphoned through a 1/4" Teflon tube into seven BOD bottles under dimmed room light. The bottles were first rinsed with the sampled water and then overflowed with the sample by ~2 times their volumes before they were closed with no headspace. During the sample transfer, the Teflon tube was inserted nearly down to the bottom of the bottles and bubbles were avoided. [CO] in one bottle was measured immediately after the sample transfer and subtracted as background [CO] in the later calculations. The remaining six bottles were incubated at constant temperatures (± 0.5°C) by immersing them in a darkened circulating water bath. They were sacrificed sequentially for [CO] measurement, usually at three time points, each in duplicate.

2.3.4. Land-based laboratory incubations

Samples brought back from the *Coriolis II* cruise were re-filtered with 0.2-μm polyethersulfone membrane filters immediately before they were incubated. The purposes

of these incubations was to determine the effects of CDOM concentration ([CDOM]), temperature (T) and pH on Q_{co}. They were performed on water samples from Stns 1, 3, 4, 12 and SF and followed exactly the same procedure as for the shipboard incubations. The [CDOM]-series study was realized by incubating samples from various stations at constant T (20.0°C) and pH (7.86), the median of the samples' original pH values. The T-series incubations were conducted at constant pH (sample's original pH) but at varying T: 2.0, 10.0, 20.0 and 30°C. The pH-series incubations were performed at constant T (20.0°C) but at pH varying from 4.0 to 10.0 (Table 4-1). HCl (1 N or 5 N) or NaOH (1 N or 5 N) was used to adjust pH, if required.

The land-based incubations were carried out within 9-26 (average: 19) d of sample collection, with each set of incubation being completed usually within 1-3 d (Table 4-1). An assessment of the effect of sample storage on Q_{co} was conducted on a surface water sample taken from Pointe- Aux-Péres, Rimouski situated on the south shore of the St. Lawrence River (Stn. PAP in Fig. 2-1). Q_{co} (20°C) in this sample was determined, using the same procedure as described above, at storage time of 1, 3, 5, 12 and 22 d. Note that [CDOM]-, T- and pH-series incubations were also performed on the PAP water (Table 4-1).

The effects of ionic strength (I) and iron on CO dark production were investigated using freshly collected, filtered RR water. To test the role of ionic strength, varying amounts of NaCl (reagent grade, BDH) were added to aliquots of the water to form an I-series of 0.0, 0.2, 0.4, 0.6 and 1.0 mol L^{-1}. Samples were then incubated at 20°C. To assess the influence of iron, the water was treated with 100 μmol L^{-1} deferoxamine mesylate (DFOM) (reagent grade, Sigma-Aldrich), a strong Fe (Zepp et al.)-complexing

ligand. The water was left in the dark for 24 h to allow the completion of the complexing process before it was incubated (20°C) along with a DFOM-free control. Incubation of Nanopure water spiked with 100 μmol L^{-1} DFOM did not produce significant CO.

2.4. Analysis.

Samples to be analyzed for CO were brought rapidly to around laboratory temperature in a water bath and a sub-sample was drawn from the bottom of the quartz cells or BOD bottles into a 50-mL glass syringe (Perfectum) via a short length of 1/8" o.d. Teflon tubing. The syringe was flushed twice with the sample water before being filled free of bubbles. The sample was analyzed using a headspace method (1:6 gas:water ratio) for CO extraction and a modified Trace Analytical TA3000 reduction gas analyzer for CO quantification (Xie et al., 2002). CDOM absorbance spectra were recorded at room temperature from 200 to 800 nm at 1 nm increments using a Perkin-Elmer lambda-35 dual beam UV-visible spectrometer fitted with 10 cm quartz cells and referenced to Nanopure water. A baseline correction was applied by subtracting the absorbance value averaged over an interval of 5 nm around 685 nm from all the spectral values (Babin et al., 2003). Absorption coefficients, a_λ (λ: wavelength in nanometers), were calculated as 2.303 times the absorbance divided by the cell's light path length in meters (Johannessen and Miller, 2001). The lower detection limit of the absorption coefficient measurement was 0.03 m^{-1}. This detection limit permitted measuring a at least up to ~600 nm for Stns. 1-10 in the estuary (a_{600}: 0.051-0.14 m^{-1}) and up to ~500 nm for Stns. 11-13 in the Gulf and Atlantic (a_{500}: 0.054-0.084 m^{-1}). Dissolved organic carbon (DOC) was measured

using a Shimadzu TOC-5050 carbon analyzer calibrated with potassium biphthalate. The coefficient of variation (c.v.) on triplicate injections was <5%. Salinity was determined with a Portasal (model 8410A) salinometer. A ThermOrion pH meter (model 420) fitted with a Ross Orion combination electrode was used to determine *pH*; the system was standardized with three NIST buffers at *pH* 4.01, 7.00, and 10.01.

Chapter 3. Photoproduction

3.1. DOM mixing dynamics.

The absorption coefficient for the original (pre-faded) samples from Stns. 1-13 decreased monotonically with increasing wavelength in UV-Visible band (Figure 3-1). Stn. 1 showed the highest absorption coefficient at each wavelength whereas Stn. 13 showed the lowest. The absolute difference among different stations is higher in the UV band and lower in the visible band.

Surface salinity (S) increased from 0.004 at Stn. 1 to 32.55 at Stn. 13. The elevated salinities at Stns. 7 and 9 were likely indicative of recently upwelled waters (Gratton et al., 1988) (Figure 3-2). The DOC and absorption coefficient (a_{350}) distributions nearly mirrored the salinity distribution. The same was true with the DOC-specific UV absorption coefficient at 254 nm ($SUVA_{254}$), an indicator of the aromatic carbon content of DOM (Weishaar et al., 2003), except at Stns. 2 and 3, where the $SUVA_{254}$ values were higher than expected considering the salinity distribution trend (Figure 3-2). The $SUVA_{254}$ vs. S curve (Figure 3-3) further confirms the presence of local DOM sources at these two sites, which are enriched with aromatic carbon relative to the DOM transported from further upstream. Since Stns. 2 and 3 were located in the maximum turbidity zone of the upper St. Lawrence estuary, local DOM inputs could be from the dissolution of trapped particulate organic materials and the injection of DOM into the water column during sediment resuspension. The release of aromatic carbon-rich

DOM from adjacent mudflats might also have contributed to the high $SUVA_{254}$ values there, especially at Stn. 3.

The a_{350} value decreased linearly with salinity, but the slope of the line changes at Stn. 6 (Figure 3-3), slightly downstream from the mouth of the Saguenay Fjord, where the topography changes abruptly from an average of ~60 m in the upper estuary to >200 m in the lower estuary. This a_{350} distribution pattern agrees with the finding by (Nieke et al., 1997). Tidal and wind-driven upwelling in and around the head of the lower estuary of CDOM-depleted deep water originating from the Atlantic Ocean (Gratton et al., 1988) could be mainly responsible for this feature. Relatively more intense in situ photobleaching in the lower estuary, as expected from the longer residence times of surface waters there, might also have played a role. However, the linear a_{350}-S relationship across the entire lower estuary suggests the absence of significant photobleaching. The [DOC]-S relationship resembles the a_{350}-S relationship except at Stn. 3, where [DOC] is lower than inferred from the DOC mixing line, resulting in the elevated $SUVA_{254}$ value at this station (Figure 3-3).

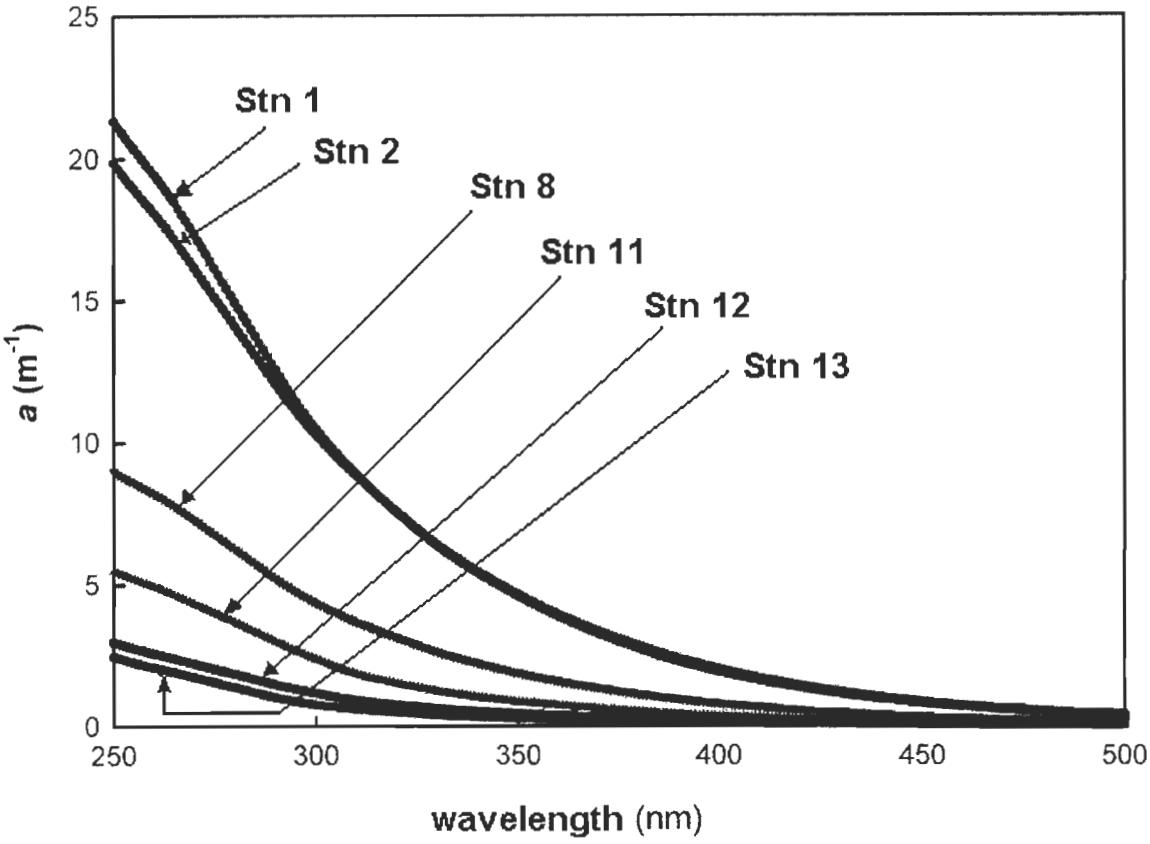

Figure 3-1. Absorption coefficient spectra for the original (not pre-faded) samples from Stns.1-13.

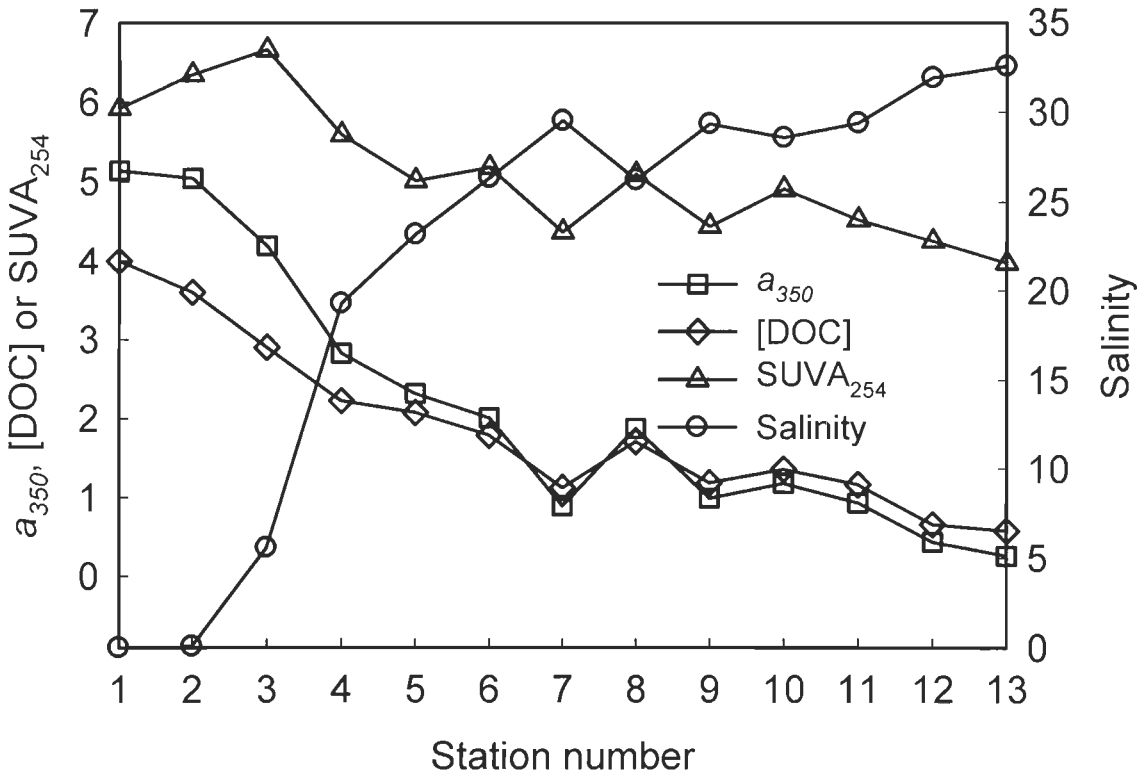

Figure 3-2. Distribution of surface-water salinity, absorption coefficient (350 nm m^{-1}), dissolved organic carbon (mg L^{-1}), and specific absorption coefficient (254 nm, L $mg^{-1}m^{-1}$) along the axial transect in the St. Lawrence estuarine system.

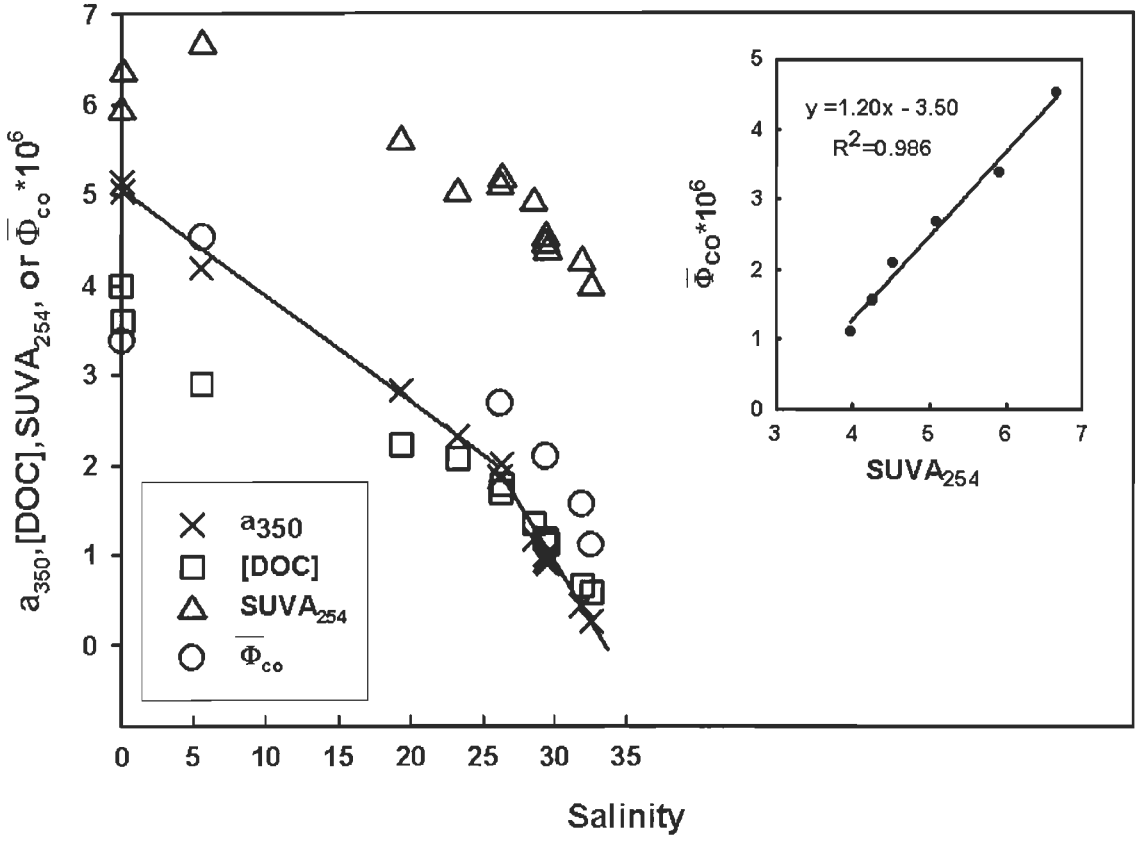

Figure 3-3. Plots of a_{350} (in m^{-1}), [DOC] (in mg L^{-1}), $SUVA_{254}$ (in L $(mgC)^{-1}$ m^{-1}), and $\overline{\Phi}_{co}$ vs salinity. The best fit of a_{350} vs salinity splits into two segments: salinity 0.0043-26.2 (y = -0.116 + 5.02, R^2 = 0.995) and salinity 26.2-32.55 (y =-0.267 + 8.86, R^2 =0.975). Inset is the $\overline{\Phi}_{co}$ vs $SUVA_{254}$ plot and the best fit. The $\overline{\Phi}_{co}$ values shown here are those determined at 15 °C on the original (not pre-faded) samples. The 15 °C temperature was chosen since the mean (± s.d.) temperature of the sampled stations was 14.2°C (± 4.4°C).

3.2. Method evaluation for modeling $\Phi_{co}(\lambda)$

3.2.1. Reproducibility of $\Phi_{co}(\lambda)$ determination

The reproducibility of the method for determining the $\Phi_{co}(\lambda)$ spectra was evaluated by running four replicate samples from Stn. 11. The coefficient of variation (c.v.) for CO photoproduction ranges from 1.1 to 12.0%, generally rising with increasing cutoff wavelength (Table 3-1). The $\Phi_{co}(\lambda)$ spectra for these replicate runs are shown in Figure 3-4. The c.v. of the four $\Phi_{co}(\lambda)$ spectra is below 2% in the 280–360 nm wavelength range and thereafter increases approximately linearly with increasing wavelength, reaching 17.5% at 600 nm (Figure 3-4). The mean (± s.d.) c.v. across the 280–600 nm range is 7.4% (± 5.6%). The c.v. of $\overline{\Phi}_{co}$ is 4.2% (Table 3-1). The latter is smaller than the former since the major production of CO occurred in the UV region (<400 nm) (see section 3.4.). Note that the performance of this method cannot be effectively evaluated with the c.v. of the individual fit parameters (Table 3-1) since both the magnitude and shape of the $\Phi_{co}(\lambda)$ spectrum is controlled by the combination of the three parameters not by their individual absolute values.

Table 3-1. Results of Replicate Measurements of Φ_{co} for Stn. 11

		Run No.				Statistic results		
	Cutoff filter	1	2	3	4	mean	s.d.	c.v. (%)
CO Photo-production rate (nmol L^{-1} h^{-1})	WG280	8.57	8.77	8.72	8.62	8.67	0.093	1.1
	WG295	5.17	5.25	5.2	5.12	5.18	0.055	1.1
	WG305	2.98	3.02	2.99	2.93	2.98	0.037	1.2
	WG320	2.51	2.46	2.56	2.57	2.53	0.050	2.0
	WG345	0.66	0.67	0.66	0.69	0.67	0.014	2.1
	GG395	0.37	0.38	0.36	0.37	0.37	0.0093	2.5
	GG435	0.1	0.1	0.09	0.1	0.10	0.0037	3.8
	GG495	0.02	0.02	0.02	0.02	0.02	0.0023	12.0
Fitting parameters of $\Phi_{co}(\lambda)$	m_1	1.18E-08	1.02E-08	1.56E-08	3.13E-08	1.72E-08	9.64E-09	56.0
	m_2	1716.2	1761.6	1591.3	1312.6	1595.4	201.8	12.7
	m_3	-100.03	-98.79	-108.70	-127.04	-108.64	13.04	-12.0
	$\overline{\Phi}_{co}*10^6$	2.04	2.01	2.09	2.21	2.09	0.09	4.2

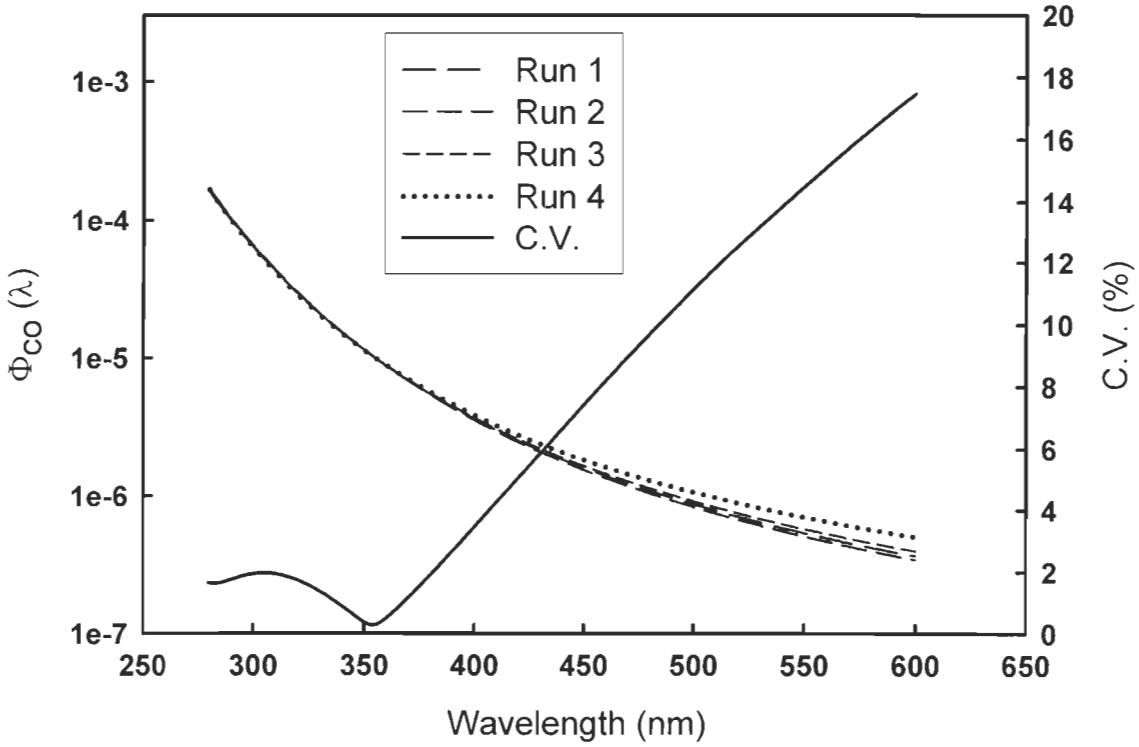

Figure 3-4. CO quantum yield spectra of four replicates from Stn. 11 and their coefficient of variation.

3.2.2. Performance of the curve fit method

The performance of the curve-fit method for deriving Φ_{co} was evaluated according to the approaches of Ziolkowski (2000) and Johannessen and Miller (2001). First, the Φ_{co} spectra derived from the curve-fit method, in conjunction with the relevant irradiance (Figure 2-3) and CDOM absorbance spectra, were used to calculate the CO production rates in the irradiation cells. Then, the calculated (or predicted) rates were plotted against the CO production rates measured in the corresponding cells, and linear regressions were performed between the two. Results from the linear regression were shown in Table 3-2. R^2 shows how well the predicted rates correlate with the measured rates. Of the total 57 runs, 19 reached $R^2 \geq 0.999$, 18 R^2 0.997–0.998, 10 R^2 0.994–0.996, 8 R^2 0.990–0.993, and 2 R^2 0.983–0.988. Figure 3-5 depicts the best and worst fits.

Table 3-2 : Results from least-squares linear regression between predicted and measured CO production rates. Regression equation: y = a*x + b. N=8 for all cases.

	Temperature series				Photobleaching series			
Stn.	T(°C)	a	b	R^2	f_{330}*	a	b	R^2
1	0.5	0.998	0.023	0.998	1.000	1.001	-0.023	1.000
	7	1.000	0.004	1.000	0.988	1.004	-0.129	0.999
	15	1.001	-0.023	1.000	0.984	0.999	-0.006	0.998
	24	1.003	-0.140	0.999	0.751	0.999	0.004	0.998
	32	1.005	-0.272	0.999	0.307	0.986	0.093	0.995
					0.169	0.986	0.055	0.995
3	0.5	0.994	0.172	0.999	1	0.995	0.169	0.999
	7	0.992	0.243	0.998	0.99	0.995	0.114	0.998
	15	0.995	0.169	0.999	0.953	1.000	-0.021	0.997
	24	0.996	0.145	0.999	0.735	0.994	0.045	0.995
	32	0.996	0.131	0.998	0.385	0.972	0.142	0.988
					0.189	0.99	0.026	0.997
8	0.5	0.997	0.022	0.999	1	0.997	0.031	0.999
	7	0.997	0.027	0.998	0.984	0.992	0.067	0.998
	15	0.997	0.031	0.999	0.981	0.992	0.060	0.997
	24	0.998	0.017	0.999	0.966	0.991	0.064	0.999
	32	1.000	0.003	0.999	0.886	0.989	0.050	0.995
					0.68	0.988	0.046	0.998
					0.424	0.983	0.036	0.996
					0.177	0.969	0.026	0.993
11	0.5	1.000	-0.002	0.999				
	7	1.001	-0.006	0.999				
	15(run1)	1.000	-0.002	0.999				
	15(run2)	1.001	-0.008	0.999				
	15(run3)	0.999	0.003	0.999				
	15(run4)	0.998	0.007	0.999				
	24	0.994	0.005	0.990				
	32	1.004	-0.048	0.997				
12	0.5	0.978	0.043	0.994	1	0.977	0.054	0.992
	7	0.979	0.046	0.995	0.886	0.982	0.034	0.993
	15	0.977	0.054	0.992	0.649	0.981	0.022	0.996
	24	0.986	0.046	0.997	0.422	0.963	0.017	0.991
	32	0.988	0.043	0.998	0.287	0.952	0.015	0.983
13	0.5	0.971	0.039	0.992	1	0.972	0.041	0.993
	7	0.981	0.030	0.997	0.943	0.980	0.030	0.994
	15	0.972	0.041	0.993	0.699	0.977	0.022	0.993
	24	0.980	0.040	0.997	0.347	0.974	0.012	0.996
	32	0.987	0.031	0.998				

*Fraction of the original absorption coefficient at 330 nm.

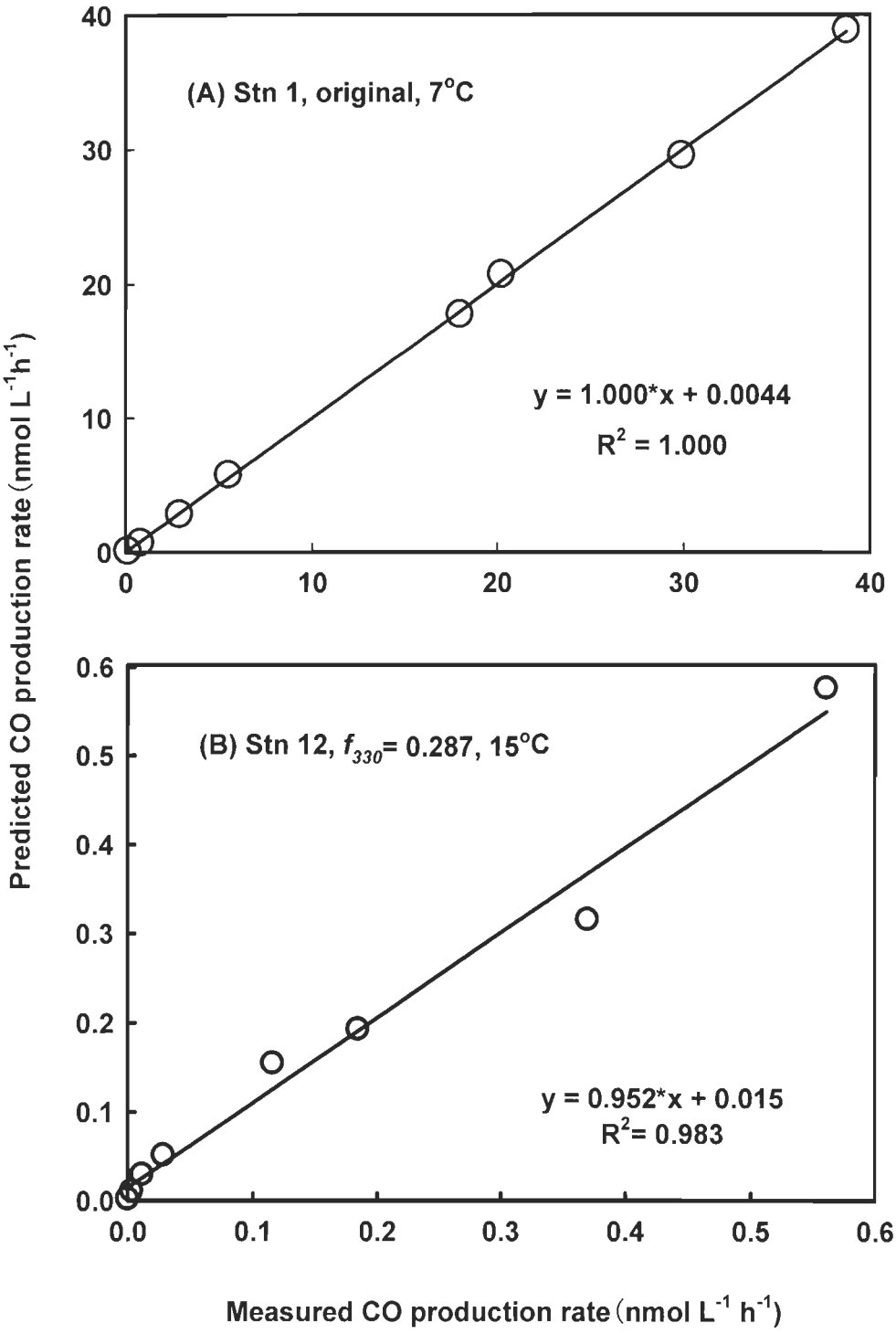

Figure 3-5. Predicted vs. measured CO production with the best (upper panel) and worst (lower panel) fits.

3.3. $\Phi_{co}(\lambda)$ spectra

A compilation of the fit parameters for $\Phi_{co}(\lambda)$ is shown in Table 3-3. All $\Phi_{co}(\lambda)$ spectra are similar in shape. $\Phi_{co}(\lambda)$ decreased with wavelength, increased with temperature, and for most stations decreased with the extent of photobleaching (f_{330}). Representative $\Phi_{co}(\lambda)$ spectra at Stn. 1 are shown in Figure 3-6.

Table 3-3. Fit parameters for function $\Phi_{co}(\lambda) = m_1 \times \exp(m_2/(\lambda+m_3))$ (eq 2-4 in the text)

	T-series				Photobleaching-series			
Stn.	T (°C)	m_1	m_2	m_3	f_{330}*	m_1	m_2	m_3
1	0.5	3.46E-11	6205.7	123.3	1.000	6.55E-10	4036.1	39.31
	7	3.81E-11	6259.2	127.1	0.988	9.91E-10	3295.1	-11.48
	15	6.55E-10	4036.1	39.31	0.984	3.40E-11	5281.2	56.62
	24	4.00E-10	4894.5	90.37	0.751	2.10E-11	5370.0	58.45
	32	1.03E-10	6969.1	195.8	0.307	9.97E-12	5401.2	45.44
					0.169	5.88E-12	5711.6	55.04
3	0.5	4.10E-11	6600.9	151.9	1.000	5.42E-11	6875.6	172.1
	7	4.53E-11	6714.2	160.2	0.990	3.72E-11	6324.2	131.9
	15	5.42E-11	6875.6	172.1	0.953	1.51E-10	4728.9	56.45
	24	6.74E-11	7332.9	205.5	0.735	1.87E-11	5800.1	88.11
	32	7.20E-11	7928.2	249.3	0.385	8.64E-12	5453.1	52.36
					0.189	1.82E-11	5019.5	47.48
8	0.5	1.12E-09	3280.0	0.00107	1.000	2.01E-09	3076.2	-6.73
	7	9.27E-11	5136.1	80.25	0.984	1.27E-11	6403.7	116.1
	15	2.01E-09	3076.2	-6.73	0.981	1.13E-11	6069.5	93.39
	24	6.20E-11	5901.4	119.2	0.966	1.04E-11	6234.2	104.2
	32	1.14E-09	3719.4	30.77	0.886	8.15E-12	6154.5	96.88
					0.680	6.35E-12	5958.3	81.88
					0.424	3.49E-11	4554.7	33.25
					0.177	6.49E-10	2738.8	-39.19
11	0.5	1.83E-08	1321.0	-133.8				
	7	3.71E-09	2097.7	-83.55				
	15	1.18E-08	1716.2	-100.0				
	24	8.77E-11	4854.9	53.97				
	32	3.61E-10	3801.4	4.68				
12	0.5	3.43E-11	5096.6	56.94	1.000	1.43E-11	5863.2	81.82
	7	2.54E-11	5400.6	68.13	0.886	2.07E-11	4943.5	31.93
	15	1.43E-11	5863.2	81.82	0.649	3.78E-10	3084.7	-33.83
	24	1.28E-11	6060.3	85.79	0.422	6.8E-09	1599.9	-102.7
	32	2.48E-11	5830.3	87.11	0.287	1.09E-08	1366.3	-119.9
13	0.5	8.38E-11	3957	-2.73	1.000	5.94E-11	4166.2	2.89
	7	1.21E-10	3545.8	-27.65	0.943	1.48E-10	3920.2	2.72
	15	5.94E-11	4166.2	2.89	0.699	7.97E-10	2920.9	-35.31
	24	3.40E-11	4690	22.10	0.347	2.43E-08	1339.4	-114.9
	32	1.02E-10	4569.1	36.88				

* Fraction of the original a_{330} values. The original a_{330} (m^{-1}) values are 6.33 (Stn. 1), 6.37 (Stn. 3), 2.6 (Stn. 8), 1.2 (Stn. 11), 0.61 (Stn. 12), and 0.38 (Stn. 13).

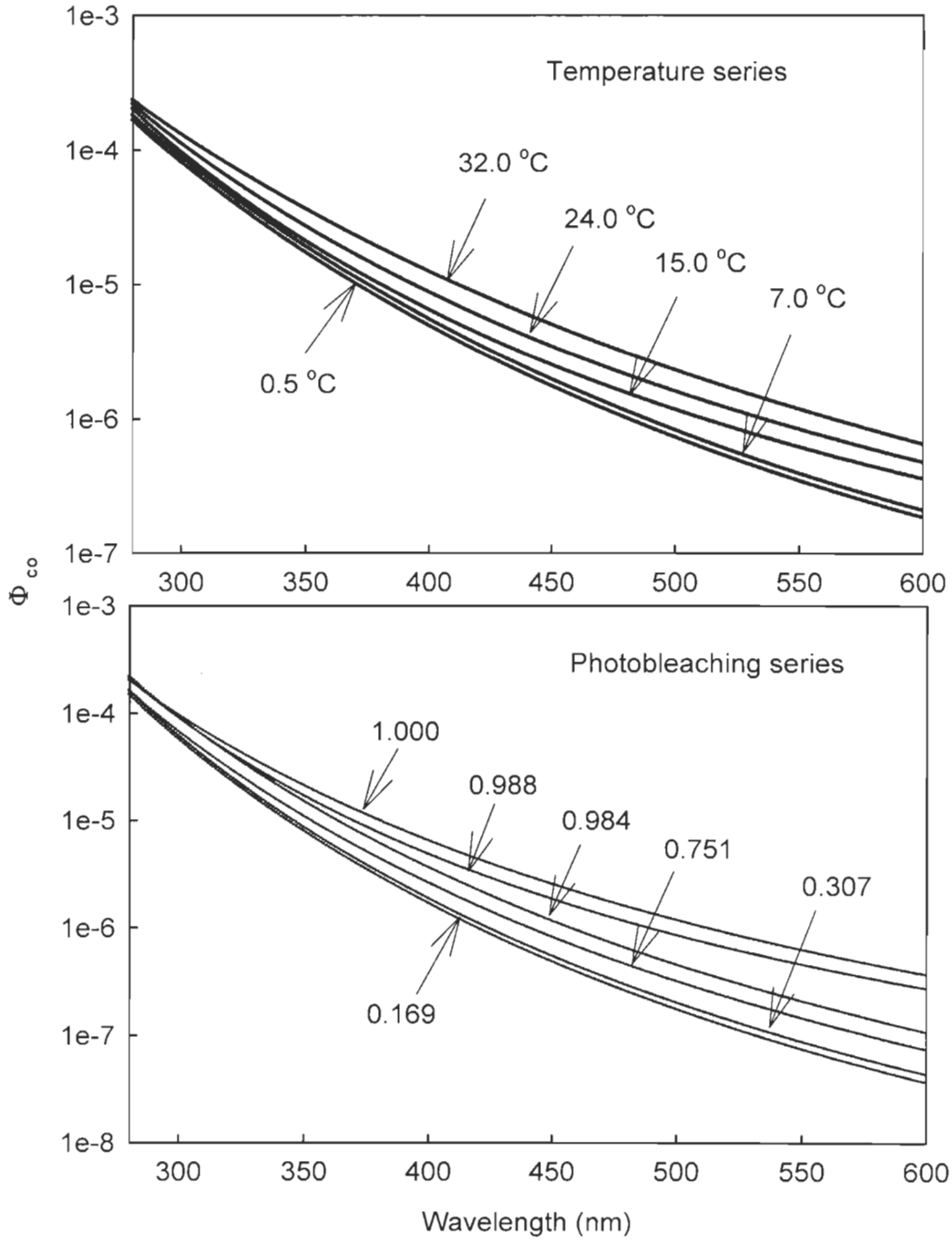

Figure 3-6. Φ_{co} spectra at Stn. 1 for temperature series (upper panel) and photobleaching series (lower panel). Numbers are irradiation temperatures (upper panel) and f_{330} (lower panel).

3.4. Response spectra of CO photoproduction

The spectral response of CO photoproduction is defined as the cross product of $Q(\lambda)$ and $\Phi_{co}(\lambda)$, where $Q(\lambda)$ is the noontime cloudless spectral solar photon flux recorded at Rimouski (48.453°N, 68.511°W), Quebec, on 24 May 2005 (Table A1). The response curve reflects the spectral distribution of depth-integrated CO photoproduction in the water column, assuming that all photochemically active solar radiations reaching the sea surface are absorbed by CDOM.

The response curves (Figure. 3-7) for varying locations (terrestrial vs. marine) and treatments (temperature variation and photobleaching) are similar in shape, with a main peak at ca. 333 nm and a minor peak at ca. 406 nm. One notable feature for Stn. 13 (the most marine sample) is that relatively more CO was produced in the visible wavelengths after the sample was pre-faded.

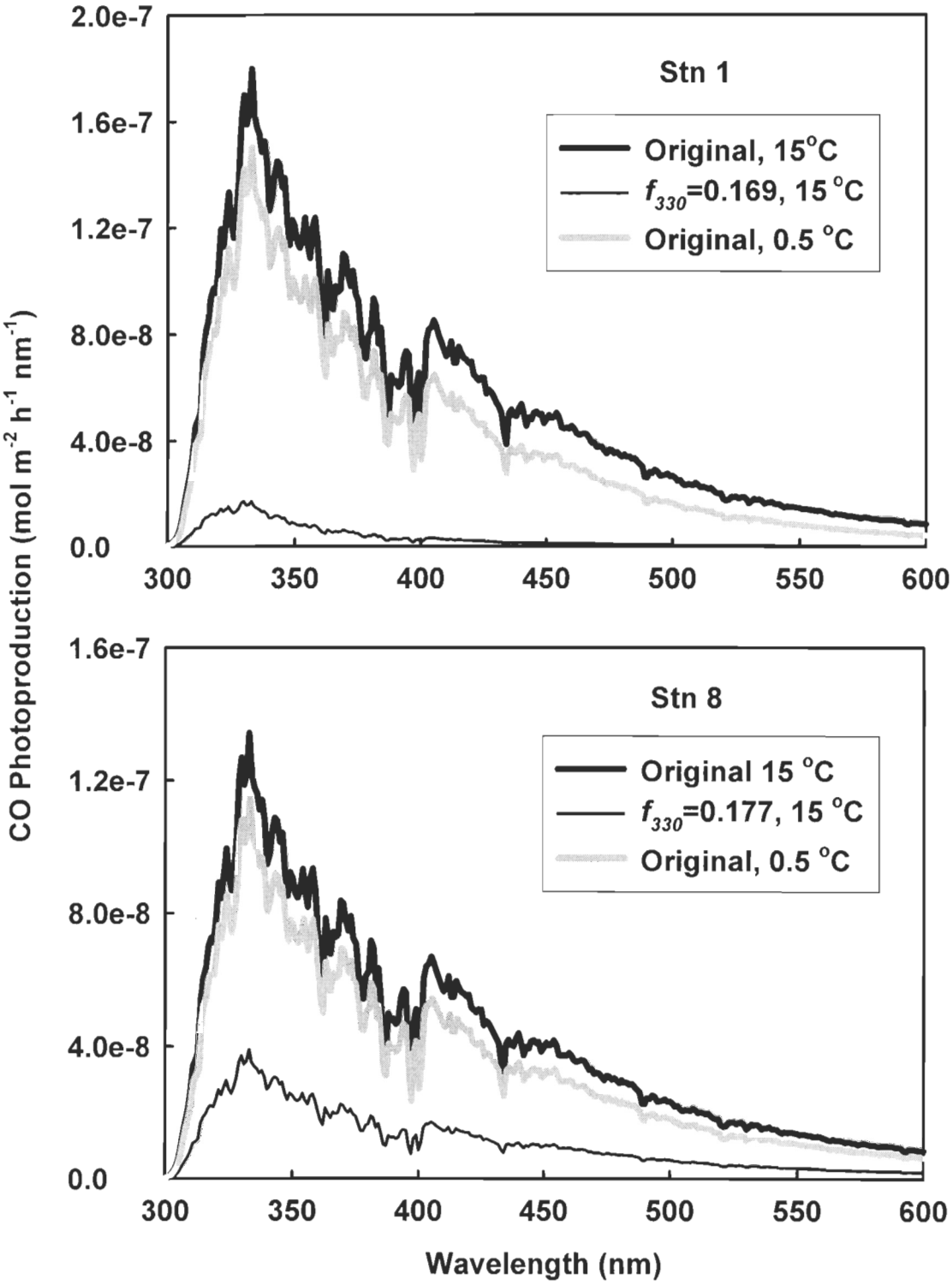

Figure 3-7.Spectral response curves of representative stations (Stns. 1, 8, 12, and 13) and treatments (original vs. photobleached sample).

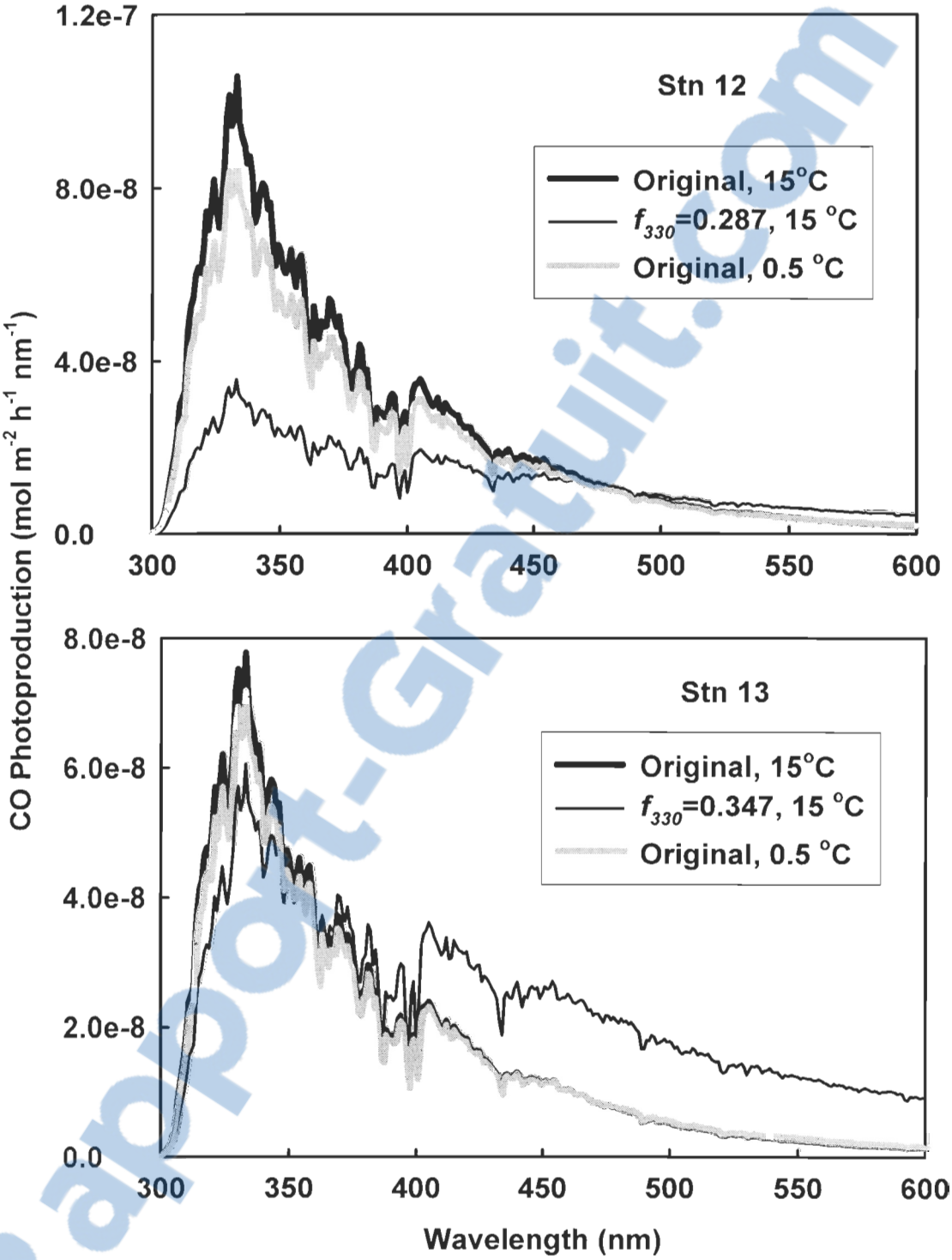

Figure 3-7. (continued)

3.5. Φ_{co} of terrestrial vs. marine CDOM.

Φ_{co} spectra representative of the upstream limit of the St. Lawrence estuary (Stn. 1), the Gulf (Stn. 11), and the Atlantic Ocean (Stn. 13) are displayed in Figure 3-8. Across the UV-visible regimes, the freshwater had the highest Φ_{co} values, the open-ocean water the lowest, and the Gulf water intermediate. However, the differences between these spectra progressively diminished with decreasing wavelength, a pattern in accordance with previous Φ_{co} spectra determined on water samples from widely varying geographic regions (Figure 3-8). These observations suggest the presence of multiple CO precursors that were less selectively photolyzed by UV-B radiation than by UV-A and visible radiation. It is also possible that metal ions (e.g., iron and copper), which are known to promote photodegradation of CDOM, could have played a role in this phenomenon since the concentrations of these metal ions are usually higher in high-CDOM estuary waters than in oceanic waters.

The spectra for the Gulf of St. Lawrence and the Atlantic Ocean almost perfectly match those for the Gulf of Maine (Ziolkowski, 2000) and the Pacific Ocean (Zafiriou et al., 2003), respectively. Nevertheless, The Φ_{co} values for the freshwater sample (Stn. 1) from the head of the St. Lawrence estuary are considerably lower, particularly in the UV-A and visible spectral regions, than those for the more colored inland lake and river waters studied by Valentine and Zepp (1993). This indicates that CDOM photoreactivity can vary substantially among freshwater ecosystems, likely due to differences in the quality of the CDOM. For example, $SUVA_{350}$ (i.e., a_{350}/[DOC]) for Valentine and Zepp's samples (2.2 L (mg C)$^{-1}$ m^{-1}) is on average 1.7 times that of our sample from Stn. 1.

$\overline{\Phi}_{co}$, as defined in eq. 2-5, increased seaward initially (from Stn. 1 to Stn. 3) but decreased monotonically with salinity downstream of Stn. 3 (Figure 3-3). Since the water mass characteristics in the Gulf are typical of Case 1 waters of oceanic origin (Nieke et al., 1997), the $\overline{\Phi}_{co}$-S relationship demonstrates that marine algae-derived CDOM is less efficient than terrestrial CDOM at producing CO photochemically. A linear regression reveals that $\overline{\Phi}_{co}$ correlates well with $SUVA_{254}$ (inset in Figure 3-3); the negative intercept suggests that not all aromatics are CO precursors. This $\overline{\Phi}_{co}$ -$SUVA_{254}$ correlation points to an important role of aromaticity in controlling $\overline{\Phi}_{co}$, which is in line with the study of Hubbard et al. (2006) demonstrating that many specific aromatic compounds are efficient CO producers. As terrestrial DOM usually contains a greater fraction of aromatic carbon than does marine DOM (Benner, 2002; Perdue and Ritchie, 2003), the higher CO production efficiency of terrestrial DOM observed in the present study is likely a general feature for aquatic environments. Mopper et al. (2006) found that increasing salinity reduced the photoreactivity of a high-CDOM swamp sample, including CO photoproduction. However, as $SUVA_{254}$ could account for 98% of the variance of $\overline{\Phi}_{co}$ (Figure 3-3), salinity was probably not a prevailing determinant of $\overline{\Phi}_{co}$ in the St. Lawrence estuary, at least for the season sampled.

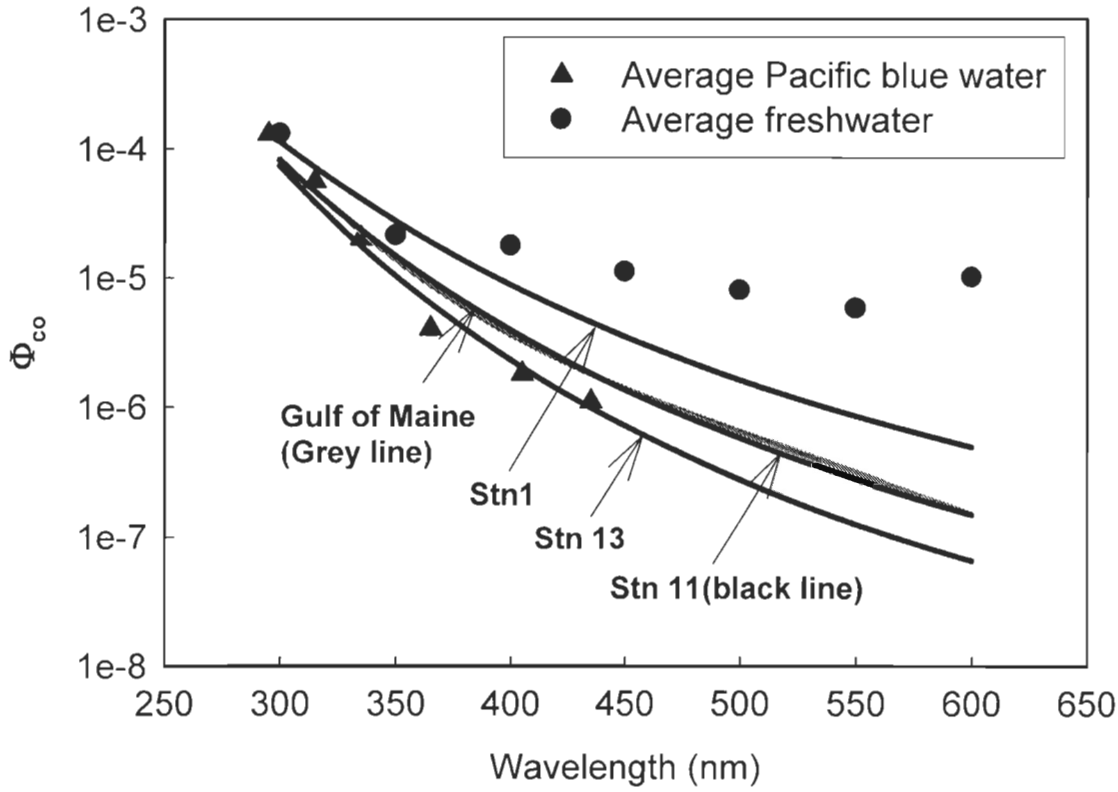

Figure 3-8. Comparison of Φ_{co} spectra for three representative stations in this study with previously published Φ_{co} spectra. The Φ_{co} spectrum for average freshwater is from Valentine and Zepp (1993), for the Gulf of Maine from Ziolkowski (2000), and for average Pacific blue water from Zafiriou et al. (2003). The spectra from this study were those determined at 24 °C on the original samples. The 24 °C temperature was chosen since irradiations for the previous studies were performed at room or laboratory temperatures (Ziolkowski, 2000, Zafiriou et al., 2003). The temperature was not reported in Valentine and Zepp (1993).

3.6. Temperature dependence.

The $\overline{\Phi}_{co}$-temperature (T) relationship followed the linear Arrhenius behavior for all stations except Stn. 13 for which a concave Arrhenius plot is evident, showing relatively constant $\overline{\Phi}_{co}$ values between 0.5 and 7 °C. (Figure 3-9). The mean activation energy for Stns. 1 and 3 in the upstream area (18.3 kJ mol^{-1}) was 78% higher than the mean activation energy for the rest of the stations (12.2 ± 0.8 kJ mol^{-1}) in the lower estuary and the Gulf. For a 20 °C increase in T, $\overline{\Phi}_{co}$ increased by approximately 70% for Stns. 1 and 3 and by 30-40% for the other stations. These changes were relatively small compared to the doubling-per-20°C T dependence of hydrogen peroxide photoproduction in Antarctic waters (Yocis et al., 2000) and dimethylsulfide photolysis in the Sargasso Sea (Toole et al., 2003), both of which are known to be secondary photoreactions (i.e., photosensitized reactions or reactions of substrates with free radicals).

The T dependence of $\overline{\Phi}_{co}$ demonstrates that secondary photoreactions were involved in the CO production, supporting the speculation by Hubbard et al. (2006) that aromatics without the carbonyl group are the dominant CO precursors but contradicting the supposition that CO is primarily produced via the direct cleavage of DOM carbonyl groups, i.e., the Norrish type I mechanism (Redden, 1982; Pos et al., 1998). However, CO production through primary photoreactions could also exist to a certain extent since simple carbonyl compounds, such as formaldehyde and acetaldehyde, with photochemical (Kieber et al., 1990) and perhaps biological (Nuccio et al., 1995) sources in natural waters, are well-known to undergo direct photodecarbonylation in the solar UV spectrum (Kagan, 2003). The lower T dependence for the saline samples suggests that

primary reactions might be more important for marine CDOM than for terrestrial CDOM, or that there was a significant difference in the secondary reaction mechanism between the two DOM pools. Since the photoproduction of carbonyl compounds from DOM is also correlated to its UV absorbance (Kieber et al., 1990), an aromatic → carbonyl compound → CO pathway, whether via primary or secondary photoreactions, agrees with the positive correlation between $\overline{\Phi}_{co}$ and aromaticity observed in the present study.

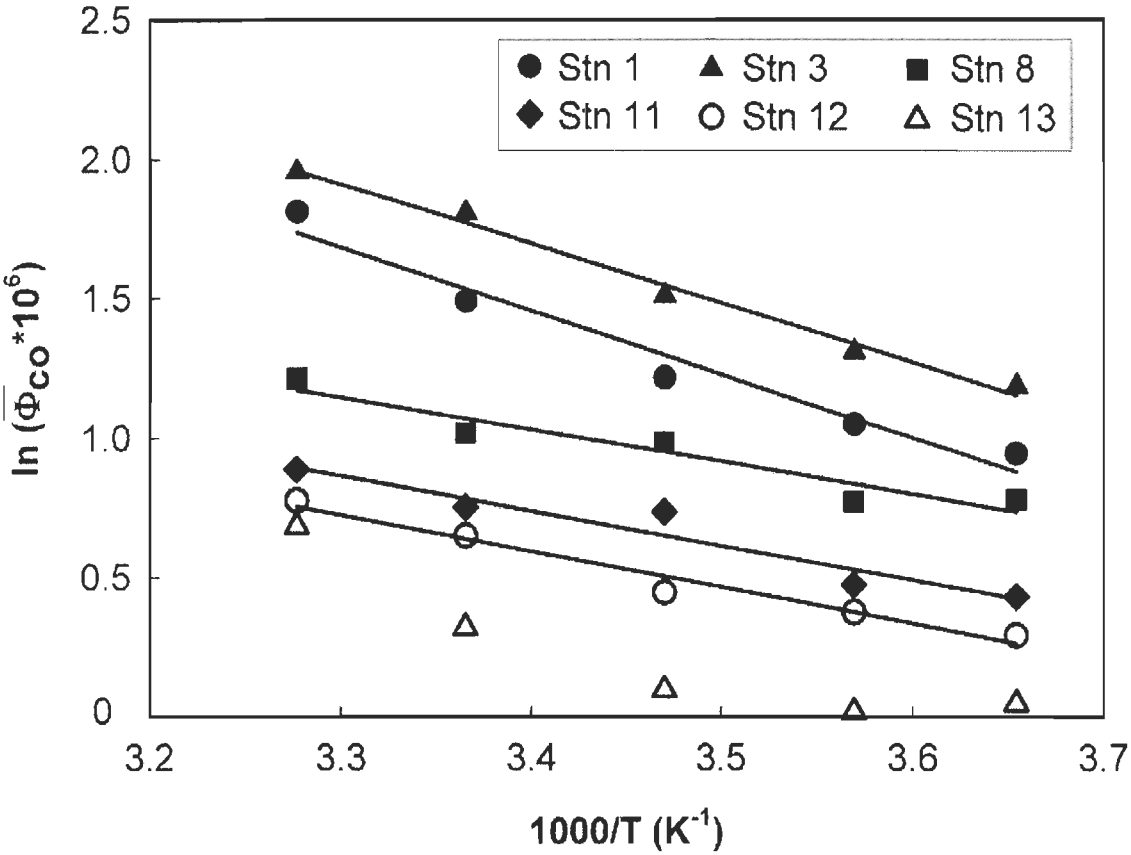

Figure 3-9. Arrhenius plots of the solar insolation-weighted mean CO quantum yield, Φ_{co}. Lines are the best fits of the data. Linear regression was not performed for Stn. 13 since its Arrhenius plot is nonlinear.

3.7. Dose dependence.

The dependence of Φ_{co} on CDOM photobleaching is depicted as plots of $\overline{\Phi}_{co}$ vs. the fraction of the original a_{330} (Figure 3-10) (note that a_{330} is selected because 330 nm is near the peak CO production wavelength as inferred from Figure 3-7). The dose dependence varied widely among different samples and at different stages of photobleaching. $\overline{\Phi}_{co}$ for the upper- and lower-estuary samples (Stns. 1, 3, and 8) decreased dramatically at first (within 5% a_{330} loss), continued to decline thereafter at gradually reducing rates, and eventually became relatively constant, a pattern resembling that of the dose dependence of photochemical O_2 consumption in diluted Shark River water (Andrews et al., 2000). Stn. 12 in the Gulf exhibited a similar pattern, but the initial decrease in $\overline{\Phi}_{co}$ was much smaller and occurred over a much broader bleaching range (over 22% a_{330} loss). Stn. 13 outside the Gulf showed no consistent dose dependence. These observations imply (1) that there appeared to be two distinct classes of CO precursors: one was very reactive, with its photolysis being faster than photobleaching, while the other was much less reactive, with its photolysis being slower than photobleaching; (2) that terrestrially derived DOM contained a much higher proportion of the reactive class relative to marine DOM. The lack of dose dependence for the most marine sample could be due to the nature of the algae-derived CDOM or to the possibility that the sample from Stn. 13 had already been considerably photobleached in situ.

Unlike the strong linear $\overline{\Phi}_{co}$-$SUVA_{254}$ correlation found for the original samples (Figure 3-3), the $\overline{\Phi}_{co}$-$SUVA_{254}$ relationship observed for the photobleaching study (Figure 3-11) is nonlinear and resembles the pattern of $\overline{\Phi}_{co}$ vs. a_{330} (Figure 3-10). This

suggests that the reactive CO precursors, as proposed above, contained aromatic moieties but that the cleavage of their aromatic rings was not required for CO production (since $SUVA_{254}$ did not decline very much during the initial rapid draw down of $\overline{\Phi}_{co}$). It also implies that the linear $\overline{\Phi}_{co}$ -$SUVA_{254}$ correlation observed for the original samples may not hold if CDOM is subjected to significant photobleaching in the environment.

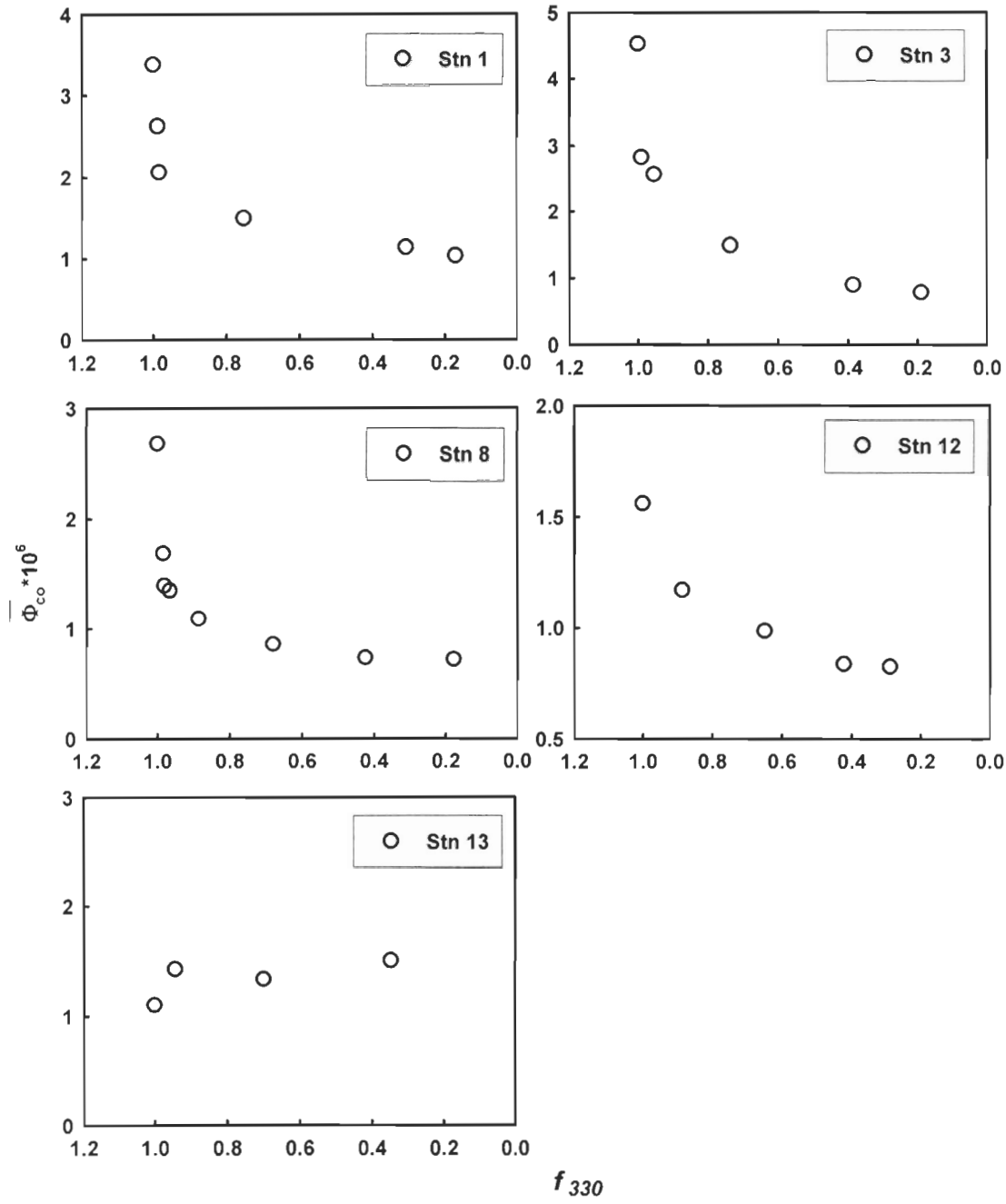

Figure 3-10. Effect of pre-fading on the CO quantum yields as illustrated by the plots of $\overline{\Phi}_{co}$ vs. f_{330} (the fraction of the original absorption coefficient at 330 nm).

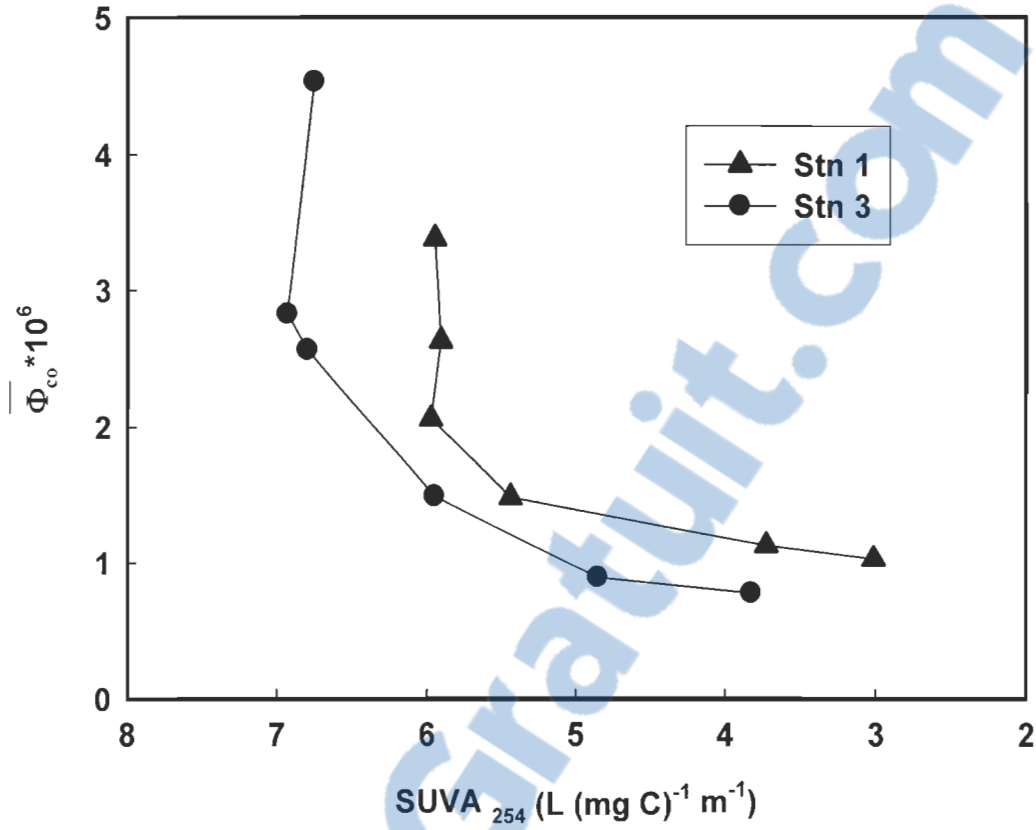

Figure 3-11. Effect of pre-fading on the CO quantum yields as illustrated by the plots of $\overline{\Phi}_{co}$ vs the specific absorption coefficient at 254 nm (Stns. 1 and 3 only; $SUVA_{254}$ data for the rest of the stations are not available).

3.8. Implication for modeling.

We are not aware of any published AQY-based modeling studies of photochemical fluxes in natural waters (Valentine and Zepp, 1993; Andrews et al., 2000; Zafiriou et al., 2003; Miller and Fichot, 2006) that have adequately taken into account the effects of the CDOM source, CDOM light history, and water temperature. Results from the present study, however, point toward the necessity of a detailed mapping of Φ_{co} in relation to these variables in order to more accurately estimate the photochemical CO fluxes and evaluate the impact of photooxidation on the cycling of marine and terrestrial DOM. Clearly, if one used freshwater samples with little prior photobleaching, Φ_{co} spectra would substantially overestimate the CO production rates in the open oceans while severe underestimation would occur if blue-water Φ_{co} spectra were applied to organic-rich estuarine and coastal areas, where DOM undergoes little photochemical processing due to limited exposure to solar radiation. Ideally, experimentally determined AQY spectra only apply to timescales over which the spectral composition and amount of solar radiation absorbed by CDOM in the field are equivalent to those absorbed by CDOM in the irradiation cells in the laboratory. Practically, it is almost not feasible to apply this approach, since it is difficult to obtain reasonably accurate information on the light history of CDOM in the field on widely varying timescales. The rapid decrease in Φ_{co} with an increasing absorbed light dose during the initial fading of the low-salinity samples indicates that using unfaded freshwater Φ_{co} spectra would strongly exaggerate the role of photochemistry in removing terrestrial DOM if CO is used as a proxy for CO_2 photoproduction. In this regard, Φ_{co} spectra determined on significantly faded samples should be employed since the faded samples showed much less dose dependence (Figure

3-10) and the initial fading, which led to the major drawdown of Φ_{co}, caused little DOC loss (< 2%). In low- and mid-latitude open oceans, CDOM in surface waters is exposed to year-round solar irradiation and the input of "fresh" CDOM is relatively slow, depending largely on the renewal of the surface waters (Siegel et al., 2002). CDOM there is expected to be significantly photobleached with respect to CO production for most of the year. This may explain why Φ_{co} spectra for widely varying open-ocean regions and different seasons are similar in both magnitude and shape (Zafiriou et al., 2003). It therefore seems acceptable to neglect the dose dependence for low- and mid-latitude blue waters (possibly with the exception of upwelling areas where unfaded CDOM in the deep ocean is transported to the surface). In high-latitude blue waters, however, the dose dependence may not be trivial at the start of the spring season, when "fresh" CDOM from the preceding long, dark winter is exposed to prolonged solar irradiation. However, if the insensitivity of CO production in our Atlantic water sample (Stn. 13) to photobleaching was a consequence of the nature of marine CDOM, then the effect of light history is likely inconsequential in blue waters regardless of locations and seasons.

The dose dependence of CO photoproduction is expected to occur on relatively short time scales and is principally restricted to interfaces (e.g., land-water interface, plant-water interface, coastal and upwelling zones, melting ice-water interface), where unexposed CDOM enters from shaded environments to unshaded ones (Vahatalo and Wetzel, 2004). In contrast, the thermal effect on this process is much milder but spatiotemporally more extensive. In mid- and high-latitude inland, estuarine, and near-shore aquatic systems, seasonal T variations can significantly influence Φ_{co}. In the St. Lawrence estuary, the summer-winter surface T difference is ~22 °C at the upstream limit

(Quebec City) and ~18 °C in the Gulf, causing Φ_{co} to be 86% and 35% higher, respectively, in summer than in winter. The effect of T seasonality in the open ocean, which is maximum in the mid-latitudes (~6 °C), is relatively small (14%) if our $\overline{\Phi}_{co}$ -T relationship for Stn. 13 is applied (the $\overline{\Phi}_{co}$ -T data were interpolated to temperatures that were not tested). Latitudinally, however, Φ_{co} spectra determined at tropical SST (annual mean T: 27.3 °C) would overestimate $\overline{\Phi}_{co}$ by 42% in the 30°-45°N (S) zone (annual mean T: 16.5 °C) and 60% in the 45-60°N (S) zone (annual mean T: 6.2 °C).

The strong linear $\overline{\Phi}_{co}$ -$SUVA_{254}$ correlation for the original samples (Figure 3-3) suggests that, for aquatic systems, in which CDOM is little photochemically processed due to self-shading, strong vertical mixing, and/or low solar insolation, $SUVA_{254}$ may serve as a predictive tool for Φ_{co}. After taking into account the T dependence, we derived the following empirical equation for predicting the CO photoproduction efficiency in the St. Lawrence estuarine system:

$$\ln(\overline{\Phi}_{co} \times 10^6) = -\frac{1626.3}{T} + 2.42 \times \ln(SUVA_{254}) + 2.62 \quad \text{.....(3-1)}$$

where $\overline{\Phi}_{co}$ is defined in eq. 2-5, T is in Kelvin, and $SUVA_{254}$ in L (mg C)$^{-1}$m^{-1}. Statistically, $SUVA_{254}$ and T can explain 96% of the variance of $\overline{\Phi}_{co}$ (Figure 3-12).

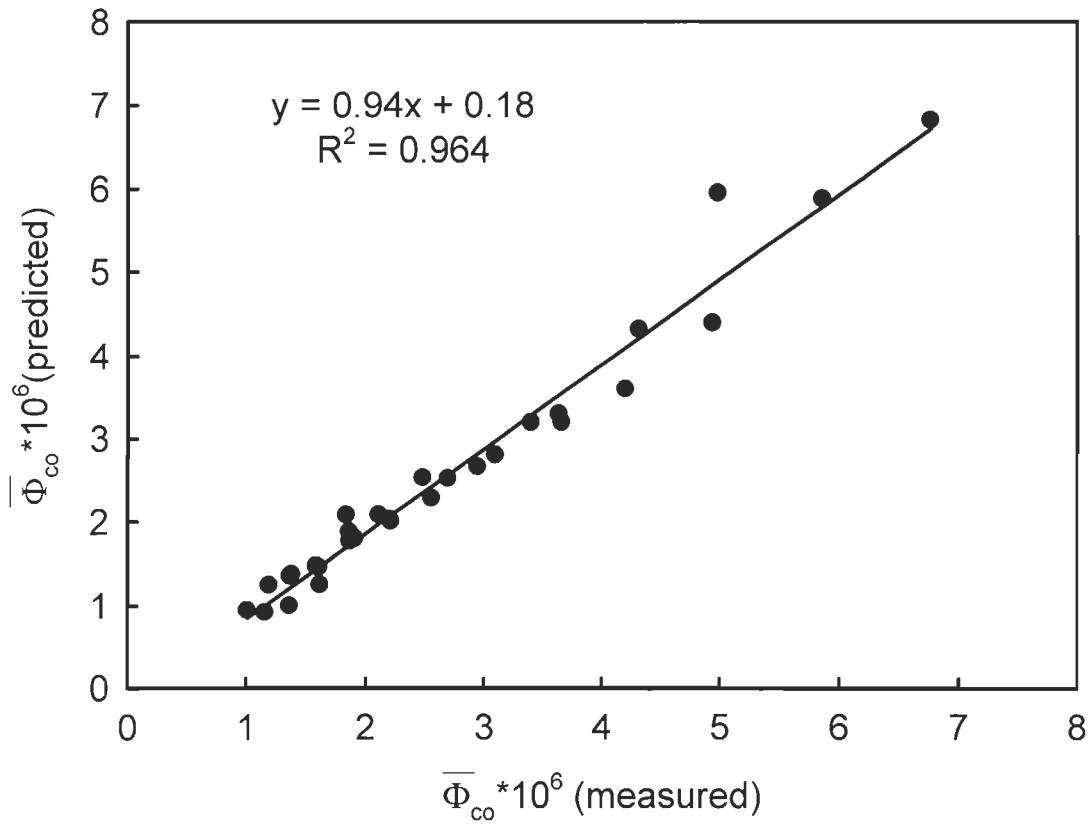

Figure 3-12. $\overline{\Phi}_{co}$ values predicted from eq. 3-1 in the main text vs. measured $\overline{\Phi}_{co}$ values. The line is the best least-squares fit of the data.

3.9. Calculation of CO photoproduction in the SLES

CO photoproduction in the water column can be calculated as follows:

$$\sum_{oceanarea} \int_{280}^{600} (irradiance \times attenuation_{1+2} \times \overline{\Phi}_{co}) d\lambda \quad \text{.....(3-2)}$$

where the attenuation factors 1 and 2 are the corrections for the reflection of light by cloud (0.8) and water (0.93) (Stubbins et al., 2006a). Light absorption by particles is not excluded since the efficiency of CO photoproduction from particles is not less than that from CDOM (Xie and Zafiriou, 2008). Therefore, CO photoproduction estimated from eq. 4-1 includes the contribution from particles, but likely at lower limits.

CO photoproductions were evaluated for each sub-region of the SLES, i.e., the Saguenay Fjord, the upper St. Lawrence estuary (USLE), the lower St. Lawrence estuary (LSLE), and the Gulf of the St. Lawrence (GSL). Seasonal means of temperature, and $SUVA_{254}$ used to calculate the seasonal means of $\overline{\Phi}_{co}$ for each sub-region were obtained from Petrie et al. (1996), Fortin and Pelletier (1995), and our St. Lawrence cruises in May 2007, July 2004, October 2005, and December 2005. Since the photochemically active zone in the SLES is usually above the mixed-layer depth, physical and optical properties in this zone are assumed to be vertically homogeneous. Seasonally averaged daily spectral global (i.e., diffuse plus direct) irradiances (280-600 nm with 1 nm increments) in the SLES (Figure A1) were generated from the SMARTS2 model (Gueymard, 1995; 2001). The inputs for the SMART2 model were listed in Table A2. The use of $\overline{\Phi}_{co}$ is justified by the fact that the relative spectral composition of the modeled solar irradiances

were similar to that of the irradiance used to compute $\overline{\Phi}_{co}$ (eq 2-5). The ratios of the former to the latter over the 280-600 nm range are (average ± s.d.):

$(2.8 \pm 1.4) \times 10^4$ in spring, $(4.0 \pm 4.6) \times 10^4$ in summer, $(1.4 \pm 0.3) \times 10^4$ in autumn, and $(7.4 \pm 2.0) \times 10^3$ in winter.

Geographically, the per-unit-area CO photoproduction rates for all four seasons, in descending order, are the Saguenay Fjord > USLE > LSLE > GSL, due mainly to the same descending trend of $\overline{\Phi}_{co}$ (Table 3-4). The area-integrated production, however, trends roughly oppositely, obviously due to the much larger areas of the GSL and LSLE than those of the Saguenay Fjord and USLE. (Table 3-4). Seasonally, all sub-regions show the highest production in summer, followed sequentially by spring, autumn, and winter, in line with the seasonal distributions of the solar irradiance (Table 3-4). It should be noted that ice and snow cover has been taken into account in the calculation of the area-integrated CO photoproduction fluxes assuming no photochemically active radiation penetrating into the under-ice water column. The ice extents used were derived from the 1971-2000 datasets of the Canadian Ice Service (2001). CO photoproduction in ice (Xie and Gosselin, 2005) was ignored since a quantitative assessment of this pathway in the SLES is not possible.

The total annual CO photoproduction in the SLES is estimated as 26.2 Gg CO-C, of which 89% is produced in the GSL with the remaining part coming almost equally from the other three sub-regions. From a seasonal perspective, summer contributes 50%, spring 26%, autumn 21%, and winter 3%.

Table 3-4. Seasonal, regional, and total CO photoproduction fluxes in the St. Lawrence Estuarine system.

Season	Region	Area[a] 10^4 km^2	T °C	$SUVA_{254}$ L (mg C)$^{-1}$ m^{-1}	$\overline{\Phi}_{co}$	Ice Coverage (%)	P_{co}[b] μmol m^{-2} d^{-1}	CO[c] Gg C
Spring	Saguenay	0.08	4.81	10.77	1.24E-05	0.83	52.8	0.05
(Mar.-May)	USLE	0.35	4.79	5.77	2.75E-06	0.11	61.2	0.23
	LSLE	0.94	1.02	4.59	1.46E-06	0.10	32.7	0.34
	GSL	22.6	0.56	4.35	1.27E-06	0.22	24.7	6.16
	Subtotal							6.78
Summer	Saguenay	0.08	17.00	10.49	1.49E-05	/	467.3	0.41
(Jun.-Aug.)	USLE	0.35	12.00	6.04	3.56E-06	/	111.3	0.43
	LSLE	0.94	5.15	4.79	1.76E-06	/	55.1	0.57
	GSL	22.6	8.31	4.37	1.51E-06	/	47.3	11.80
	Subtotal							13.21
Autumn	Saguenay	0.08	9.00	10.22	1.19E-05	/	168.1	0.15
(Sep.-Nov.)	USLE	0.35	8.00	6.32	3.66E-06	/	51.5	0.20
	LSLE	0.94	3.57	4.53	1.49E-06	/	21.0	0.22
	GSL	22.6	7.56	4.29	1.42E-06	/	20.0	4.99
	Subtotal							5.55
Winter	Saguenay	0.08	0.00	10.12	9.66E-06	0.92	5.9	0.00
(Dec.-Feb.)	USLE	0.35	-0.30	6.24	2.97E-06	0.65	8.0	0.02
	LSLE	0.94	0.13	4.55	1.40E-06	0.60	4.3	0.02
	GSL	22.6	0.65	4.28	1.22E-06	0.45	5.2	0.64
	Subtotal							0.68
	Grand total							26.2

[a] The areas of USLE and LSLE are from d'Anglejan (1990), the area of GSL from Gearing and Pocklington (1990), and the area of the Saguenay Fjord from Schafer et al. (1990).

[b] P_{co} stands for CO photoproduction rate.

[c] Effect of ice coverage has been taken into accounted.

Chapter 4. Dark production

4.1. Incubation results

In incubations where significant CO dark production was detected (53 out of 57 incubations total), [CO] always increased linearly with time over incubation durations. The Q_{co} values derived from least-squares regression analysis between [CO] and incubation time are included in Table 4-1. Plots of [CO] vs. incubation time and parameters for the best fit equations are given in Figure 4-1 and Table 4-2. A t-test indicated that even the lowest slope in Figure 4-1 is significantly different from zero, showing that all dark production rates are significant.

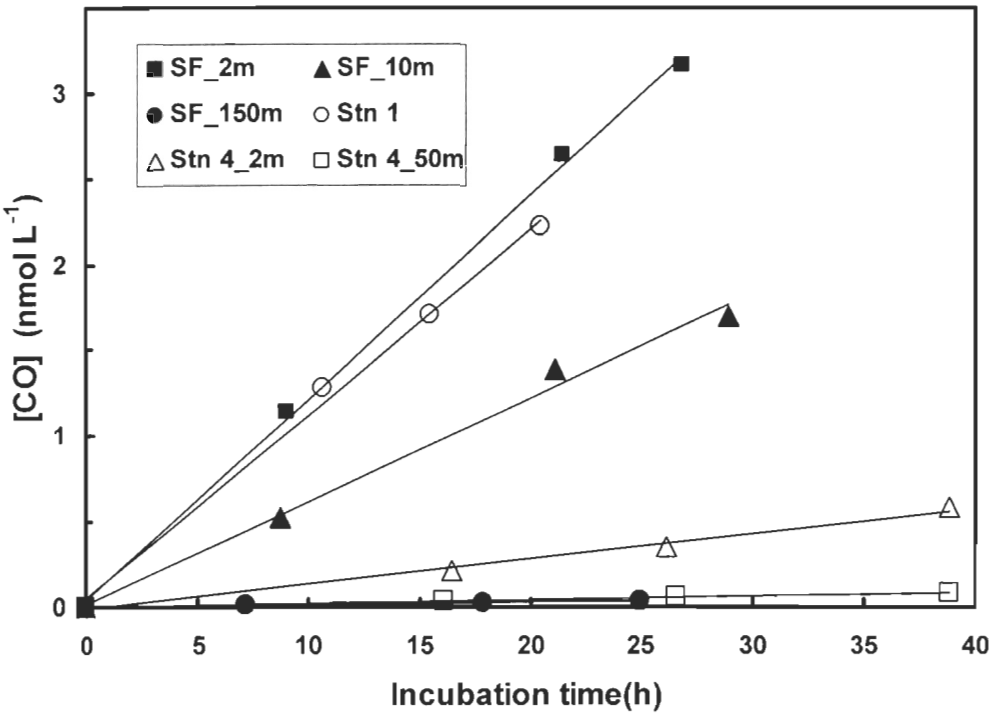

Figure 4-1A. Plot of [CO] vs incubation time in the shipboard incubations.

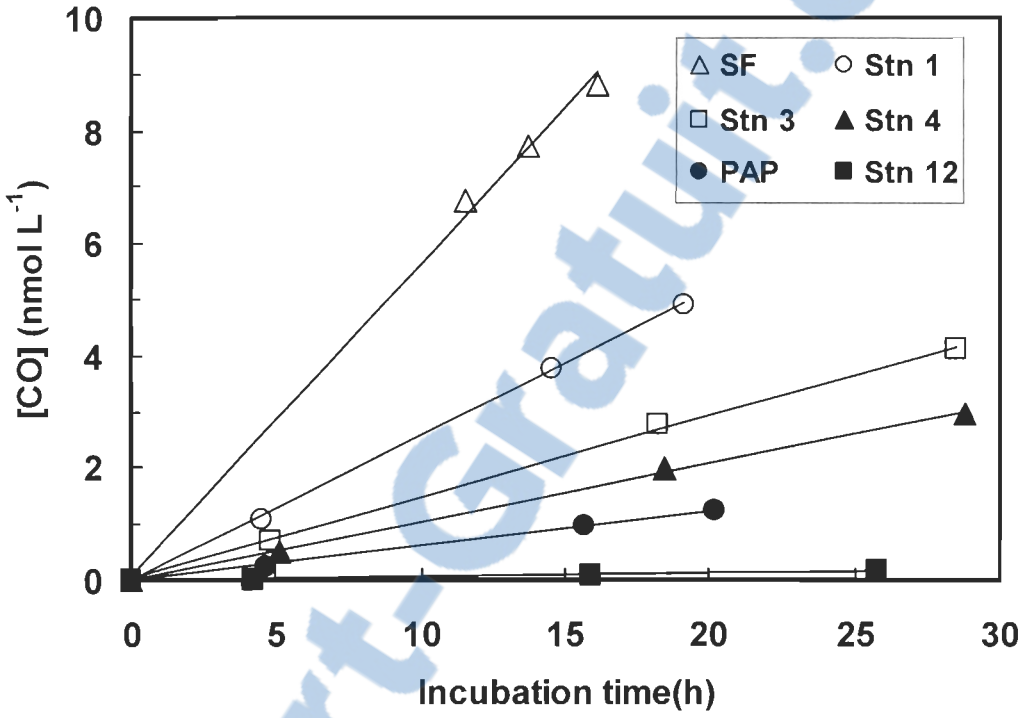

Figure 4-1B. Plot of [CO] vs. incubation time in the [CDOM]-series incubation

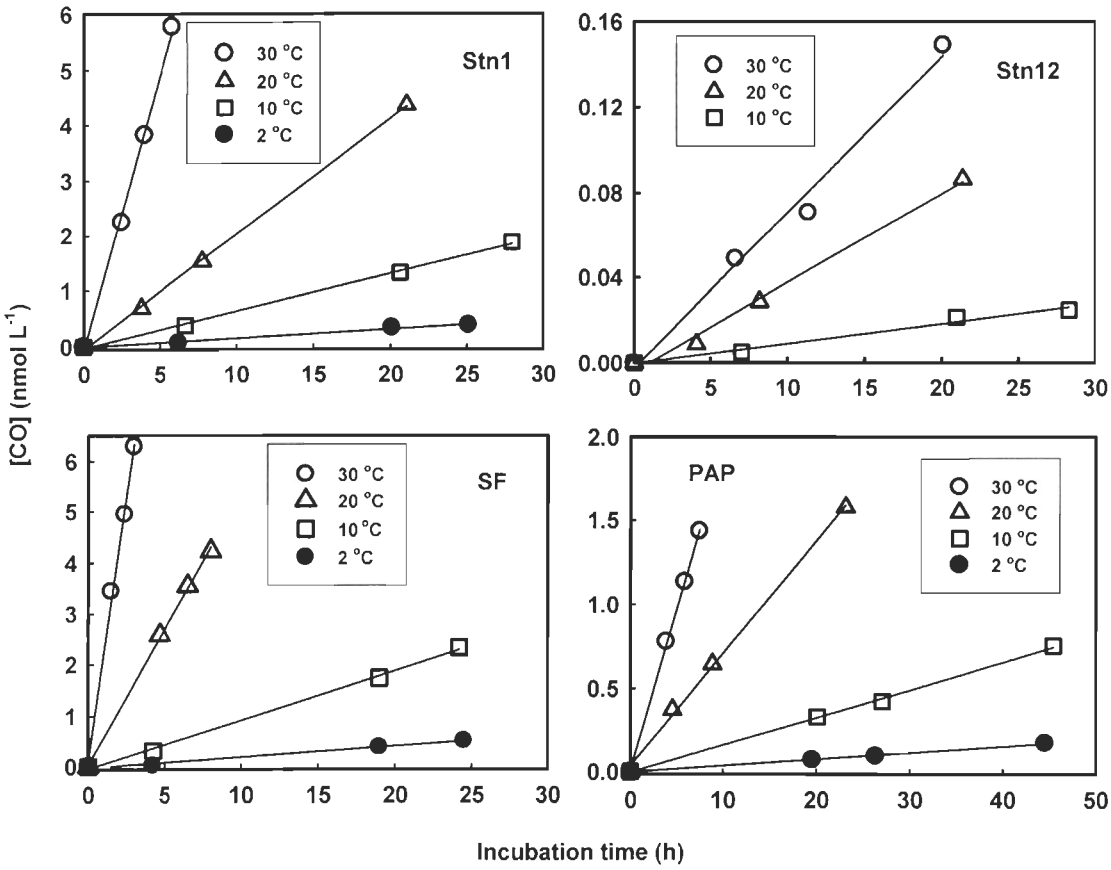

Figure 4-1C. Plot of [CO] vs. incubation time in the temperature-series incubation.

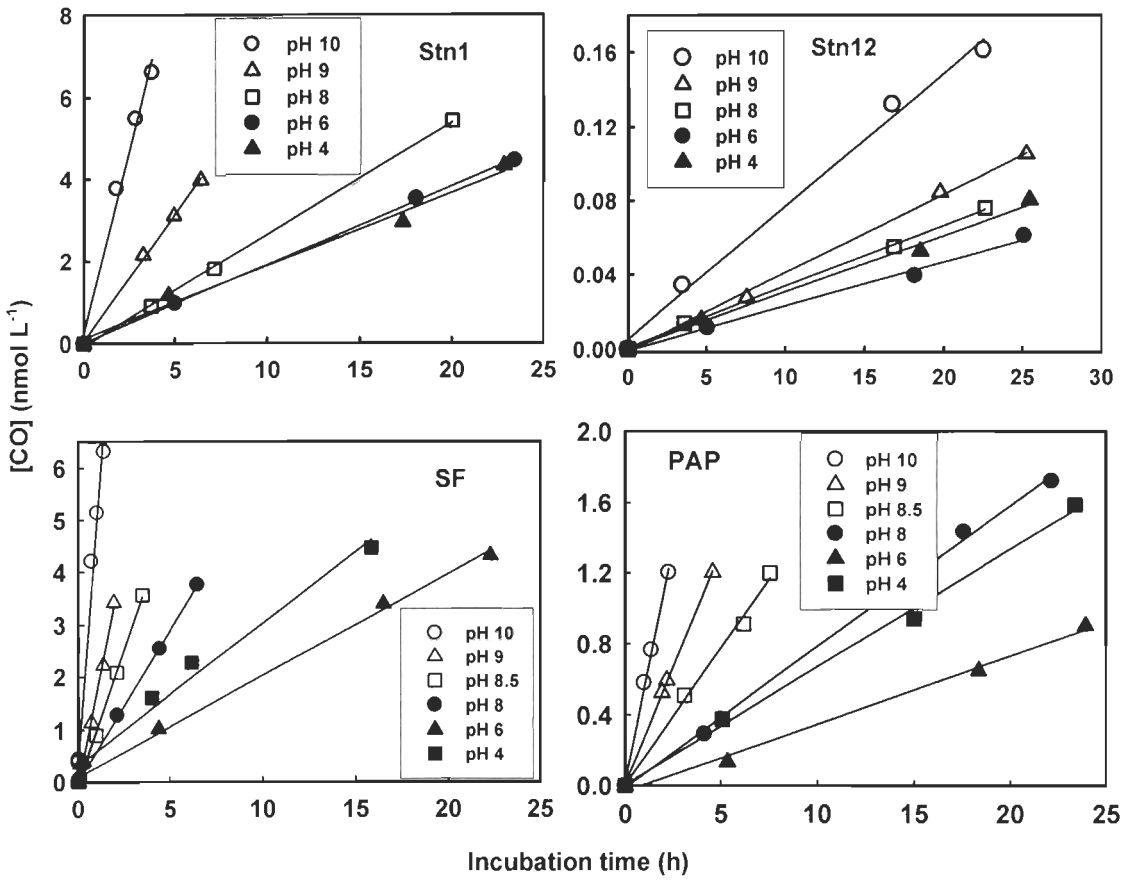

Figure 4-1D. Plot of [CO] vs. incubation time in the pH-series incubation

Table 4-1. Stations, sampling depth, water temperature (T), salinity, pH, a_{350}, dark production rate (Q_{co}), and sample storage time.

Incubation	Stn.	Depth (m)	T (°C)	Salinity	pH	a_{350} (m^{-1})	Q_{co} (nmol L^{-1} h^{-1})	Storage time (d)
Shipboard analysis	1	2	9.49	0.1	7.76	6.80	0.11	0
	4	2	3.70	18.5	7.81	3.36	0.015	0
	4	50	0.91	29.1	7.79	1.31	0.0021	0
	12	2	1.94	31.6	8.10	0.56	u.d.*	0
	12	20	0.30	31.9	8.00	0.56	u.d.*	0
	12	300	5.42	34.7	7.75	0.23	u.d.*	0
	SF	2	5.54	4.7	7.59	15.32	0.12	0
	SF	10	2.00	20.6	7.55	8.03	0.060	0
	SF	150	1.68	31.1	7.62	1.42	0.0015	0
[CDOM]-series	12	2	20.0	31.6	7.86	0.56	0.0059	11
	4	2	20.0	18.5	7.86	3.36	0.10	9
	3	2	20.0	12.9	7.86	4.21	0.15	9
	1	2	20.0	0.1	7.86	6.80	0.26	11
	SF	2	20.0	4.7	7.86	15.32	0.55	9
	PAP	0	20.0	25.6	7.86	2.42	0.062	15
T-series	12	300	2.0	34.7	7.75	0.23	u.d.*	18
	12	300	10.0	34.7	7.75	0.23	0.0009	18
	12	300	20.0	34.7	7.75	0.23	0.0042	19
	12	300	30.0	34.7	7.75	0.23	0.0073	19
	1	2	2.0	0.1	7.76	6.80	0.016	15
	1	2	10.0	0.1	7.76	6.80	0.067	15
	1	2	20.0	0.1	7.76	6.80	0.21	16
	1	2	30.0	0.1	7.76	6.80	0.99	16
	SF	2	2.0	4.7	7.59	15.32	0.022	16
	SF	2	10.0	4.7	7.59	15.32	0.097	16
	SF	2	20.0	4.7	7.59	15.32	0.53	17
	SF	2	30.0	4.7	7.59	15.32	2.08	17
	PAP	0	2.0	25.6	7.97	2.42	0.0038	19
	PAP	0	10.0	25.6	7.97	2.42	0.016	19
	PAP	0	20.0	25.6	7.97	2.42	0.067	20
	PAP	0	30.0	25.6	7.97	2.42	0.19	20
pH-series	12	300	20.0	34.7	4.00	0.23	0.0031	25
	12	300	20.0	34.7	6.00	0.23	0.0024	25
	12	300	20.0	34.7	8.00	0.23	0.0033	25
	12	300	20.0	34.7	9.00	0.23	0.0042	26
	12	300	20.0	34.7	10.00	0.23	0.0072	26
	1	2	20.0	0.1	4.00	6.80	0.18	24
	1	2	20.0	0.1	6.00	6.80	0.19	24
	1	2	20.0	0.1	8.00	6.80	0.27	24
	1	2	20.0	0.1	9.00	6.80	0.62	25
	1	2	20.0	0.1	10.00	6.80	1.81	25
	SF	2	20.0	4.7	4.00	15.32	0.27	26
	SF	2	20.0	4.7	6.00	15.32	0.19	26
	SF	2	20.0	4.7	8.00	15.32	0.58	26
	SF	2	20.0	4.7	8.50	15.32	1.03	26
	SF	2	20.0	4.7	9.00	15.32	1.76	26
	SF	2	20.0	4.7	10.00	15.32	4.55	26
	PAP	0	20.0	25.6	4.00	2.42	0.066	15
	PAP	0	20.0	25.6	6.00	2.42	0.038	15
	PAP	0	20.0	25.6	8.00	2.42	0.08	15
	PAP	0	20.0	25.6	8.50	2.42	0.15	15
	PAP	0	20.0	25.6	9.00	2.42	0.26	15
	PAP	0	20.0	25.6	10.00	2.42	0.53	15

* undetectable

Table 4-2. Results from least-squares linear regression between CO dark production and incubation time. Regression equation: $y = a \times x + b$. N = 4 for all cases.

Incubation	Stn.	Depth(m)	T (°C)	pH	*a*	b	R^2
Shipboard	1	2	9.49	7.76	0.11	0.046	0.995
analysis	4	2	3.70	7.81	0.015	-0.017	0.991
	4	50	0.91	7.79	0.0021	-0.001	0.997
	SF	2	5.54	7.59	0.12	0.035	0.999
	SF	10	2.00	7.55	0.060	0.017	0.991
	SF	150	1.68	7.62	0.0015	0.0001	0.991
[CDOM]-	12	2	31.6	7.86	0.0059	-0.0074	0.965
series,	4	2	18.5	7.86	0.10	-0.0003	0.999
	3	2	12.9	7.86	0.15	0.0204	0.999
	1	2	0.1	7.86	0.26	-0.0189	1.000
	SF	2	4.1	7.86	0.55	0.0827	0.997
	PAP	0	25.6	7.86	0.062	-0.018	0.999
T-series	12	300	10.0	7.75	0.0009	-0.0003	0.983
	12	300	20.0	7.75	0.0042	0.0042	0.992
	12	300	30.0	7.75	0.0073	-0.0025	0.988
	1	2	2.0	7.76	0.016	-0.013	0.988
	1	2	10.0	7.76	0.067	-0.035	0.998
	1	2	20.0	7.76	0.21	-0.062	0.999
	1	2	30.0	7.76	0.99	-0.092	0.998
	SF	2	2.0	7.59	0.022	-0.034	0.986
	SF	2	10.0	7.59	0.097	-0.049	0.998
	SF	2	20.0	7.59	0.53	0.032	0.999
	SF	2	30.0	7.59	2.08	0.10	0.996
	PAP	0	2.0	7.97	0.0038	-0.003	0.996
	PAP	0	10.0	7.97	0.017	-0.005	0.997
	PAP	0	20.0	7.97	0.067	0.034	0.997
	PAP	0	30.0	7.97	0.19	0.009	0.999
pH-series	12	300	20.0	4.00	0.0031	-0.0005	0.994
	12	300	20.0	6.00	0.0024	-0.0009	0.992
	12	300	20.0	8.00	0.0033	0.0007	0.996
	12	300	20.0	9.00	0.0042	-0.0014	0.997
	12	300	20.0	10.00	0.0072	0.0051	0.993
	1	2	20.0	4.00	0.18	0.11	0.987
	1	2	20.0	6.00	0.19	0.018	1.000
	1	2	20.0	8.00	0.27	-0.074	0.999
	1	2	20.0	9.00	0.62	0.046	0.999
	1	2	20.0	10.00	1.81	0.23	0.988
	SF	2	20.0	4.00	0.27	0.32	0.976
	SF	2	20.0	6.00	0.19	0.10	0.997
	SF	2	20.0	8.00	0.58	0.012	1.000
	SF	2	20.0	8.50	1.03	-0.053	0.999
	SF	2	20.0	9.00	1.76	-0.066	0.996
	SF	2	20.0	10.00	4.55	0.33	0.971
	PAP	0	20.0	4.00	0.066	0.018	0.996
	PAP	0	20.0	6.00	0.038	-0.033	0.993
	PAP	0	20.0	8.00	0.080	-0.011	0.997
	PAP	0	20.0	8.50	0.15	0.0068	0.995
	PAP	0	20.0	9.00	0.26	0.010	0.999
	PAP	0	20.0	10.00	0.53	0.023	0.997

4.2. Spatial distribution of Q_{co}

Samples for shipboard incubations spanned a relatively small *pH* range (7.55-8.10), an intermediate *T* range (0.30-9.49°C), and large variations of salinity (0.1-34.7) and [CDOM] (a_{350}: 0.23-15.32m^{-1}) (Table 4-1). They covered various water masses represented by highly colored riverine water at Stn. SF (2 m), relatively "white" freshwater at Stn. 1, estuarine water at Stn. 4 (2 m) and PAP, coastal water at Stn. 12 (2 m), and largely oceanic water at Stn.12 (300 m) (Fig. 2-1). As these samples were incubated at in situ *T* and *pH*, their Q_{co} values are considered to approximate in situ rates. In the surface mixed layer, Q_{co} (2 m deep) was the highest (0.12 nmol L^{-1} h^{-1}) in the Saguenay Fjord (Stn. SF), decreased progressively from the upstream limit of the SLES (Stn. 1: 0.11 nmol L^{-1} h^{-1}) to the Gulf (Stn. 12: undetectable) (Table 4-1), in accordance with the descending [CDOM] and *T* toward the sea. Vertically, Q_{co} dropped by ~7 times from 2 to 50 m at Stn. 4, and by 2 times from 2 to 10 m and ~92 times from 2 to 150 m at SF. The decrease in Q_{co} with depth was in line with the vertical distributions of [CDOM] and *T* (Table 4-1). These Q_{co} profiles are similar to those of carbonyl sulfide (COS) dark production in the Northeast Atlantic, which is approximately one order of magnitude weaker in deep waters than in the mixed layer (Flock and Andreae, 1996). CO dark production was undetectable at all three depths sampled at Stn. 12 due apparently to the combination of low CO precursor concentrations (as reflected by low [CDOM]) and low water *T* (Table 4-1).

4.3. Factors affecting CO dark production

4.3.1. Q_{co} vs. [CDOM]

For samples whose Q_{co} was determined at fixed T and pH ([CDOM]-series in Table 4-1), Q_{co} should be dictated by the abundance and reactivity of CO precursors, ionic strength, and other chemical variables (e.g., certain metal ions) that could influence the thermal reactions responsible for generating CO. Statistical analysis indicates that a_{350} accounts for 99.7% of the Q_{co} variability (Fig. 4-2), suggesting that organic substrates were a prevailing factor in controlling CO dark production and that [CDOM] is a good proxy of the abundance of CO precursors. This leaves ionic strength and other chemical variables to be minor factors, as confirmed by separate tests (see below). The [CDOM]-normalized Q_{co}, β_{co}, decreased with salinity (Fig. 4-2), pointing to CO precursors of marine origin being less efficient than their terrestrial counterparts. This observation is similar to that for the photoreactivity of CDOM with respect to CO photoproduction (see section 3.5.). The convex shape of the β_{co} vs. salinity (S) curve implies that, besides dilution, other unidentified factors impacted β_{co}. The anti-variation between β_{co} and S are at least partly responsible for the negative intercept in the fit equation of Q_{co} vs. a_{350} (Fig. 4-2) since low-S, high-β_{co} samples were also enriched with [CDOM], tilting the line upwards with increasing a_{350}.

In principle, dissolved organic carbon (DOC) could be a better proxy than CDOM for CO precursors since CDOM is only a portion (though usually a large portion in estuarine and coastal waters) of the whole DOM pool. Unfortunately, instrumental

problems occurring in the DOC analysis resulted in no reliable DOC data from this study. The excellent correlation between Q_{co} and a_{350}, however, suggests that CO precursors were mainly present in CDOM or that [CDOM] linearly correlated with the DOC concentration. Similarly, Von Hobe et al. (2001) found CDOM (a_{350}) also to be a good indicator of organic substrates for COS dark production in the Sargasso Sea.

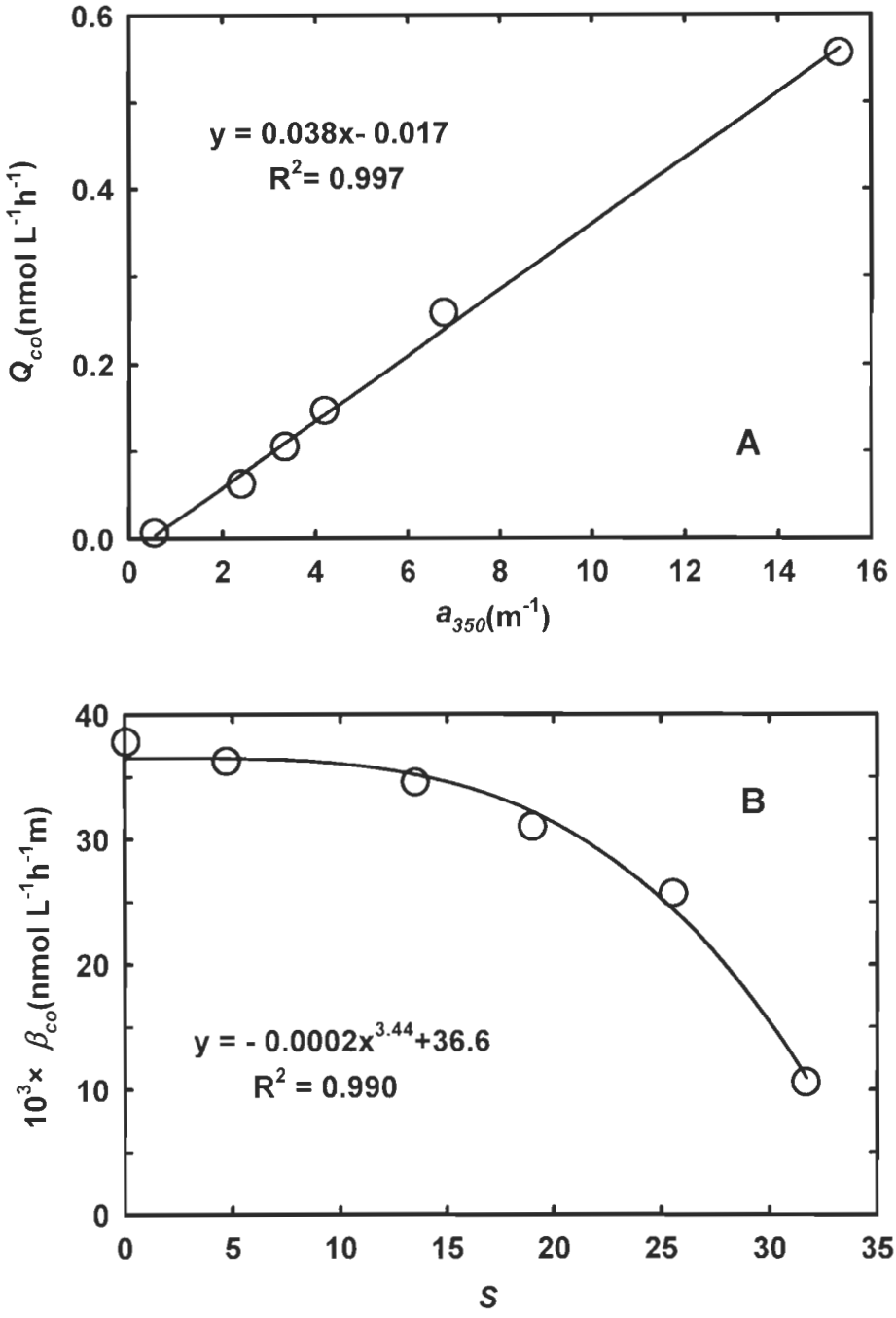

Figure 4-2. (A) Dark production rate, Q_{co}, as a function of CDOM absorption coefficient at 350 nm, a_{350}. Line is the best fit of the data; (B) the CDOM-normalized CO dark production rate, β_{co} (i.e., $Q_{co} \div a_{350}$), as a function of salinity, S. Q_{co} was determined at $pH = 7.86$ and $T = 20^{o}C$.

4.3.2. Temperature dependence.

Assessment of the T effect on CO dark production was made on four water samples from Stns. 1 (2 m), SF (2 m), PAP (0 m) and Stn. 12 (300 m) representing four differing water masses (see section 4.2.). Significant CO dark production was found in all incubations except for the Stn. 12 sample incubated at 2.0 °C (T-series in Table 4-1) due obviously to low temperature. As expected, the Q_{co}–T relationship follows the linear Arrhenius behavior (Fig. 4-3). The activation energy, E_a, in ascending order, is Stn. 12 (75.1 kJ mol^{-1}), PAP (96.4 kJ mol^{-1}), Stn. 1 (97.5 kJ mol^{-1}), and SF (113.0 kJ mol^{-1}). E_a for freshwater samples is therefore considerably higher than for the most saline water (Stn. 12), a trend similar to that found for E_a of CO photoproduction (see section 3.6.). However, E_a of dark production is much higher than that of photoproduction (<20 kJ mol^{-1}). For a 20°C increase in T, CO dark production should increase by ~22 times at Stn. SF, ~16 times at Stns. 1, and ~8 times at Stn. 12. In contrast, a similar elevation of T would raise CO photoproduction merely by <70%.

In the SLES, the summer-winter surface T difference is ~22°C at the upstream limit (Quebec City) and ~18°C in the Gulf, causing Q_{co} to be 22 times and 6 times higher, respectively, in summer than in winter. Similar seasonal T-driven variations in CO dark production are expected for mid- and high-latitude inland, estuarine, and near-shore aquatic systems. However, the effect of T seasonality in the open ocean, maximal in mid-latitudes (~6°C), should be relatively small (~2 times) if our Q_{co}-T relationship for Stn. 12 is applied.

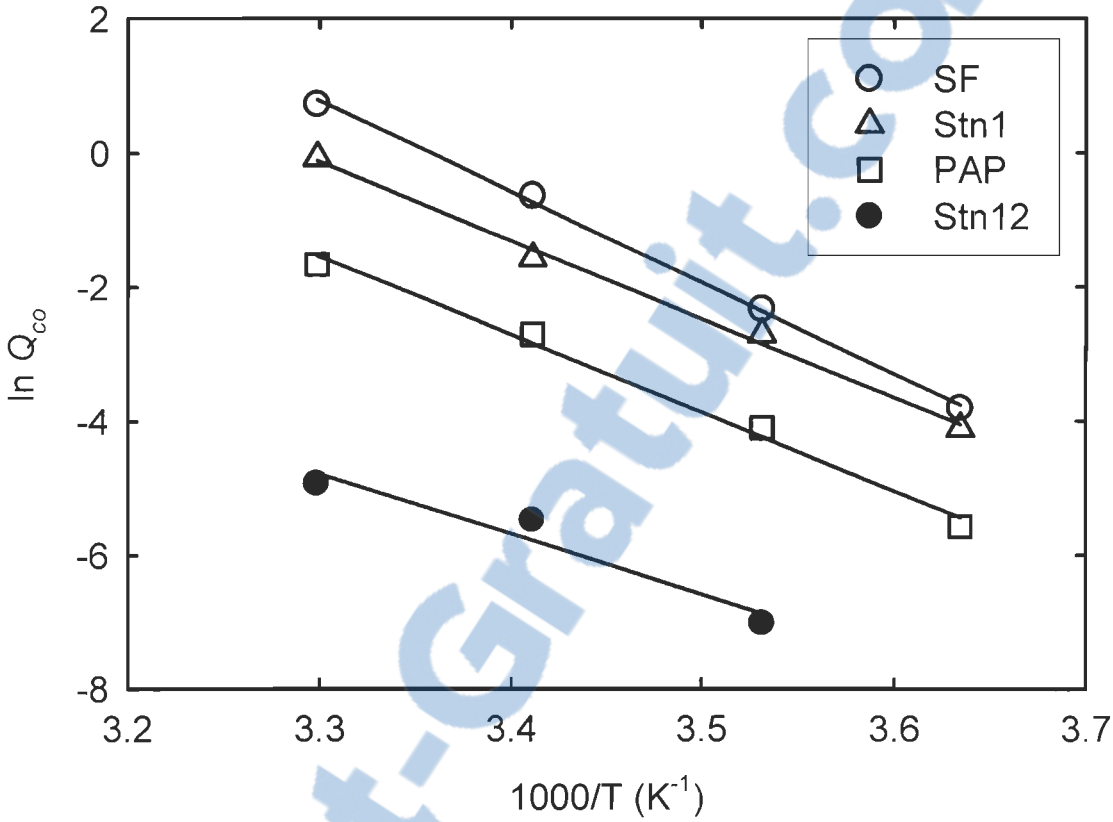

Figure 4-3. Arrhenius plots of CO dark production rates. Q_{co} was determined at sample's original *pH*. Lines are the best fits of the data.

4.3.3. Effect of *pH*

The same samples examined for the *T* effect were used to assess the *pH* effect. The shapes of all four Q_{co} vs. *pH* curves are alike (Fig. 4-4). From *pH* 4.0 to 6.0, Q_{co} slightly decreased at Stns. 12, PAP, and SF while remained stable at Stn. 12. The production rate went up slowly from *pH* 6.0 to 8.0 and then rapidly with further increasing *pH*. Mopper et al. (2006) observed a similar *pH*-dependence of CO photoproduction in a CDOM-rich swamp sample, showing minimum photoproduction in *pH* 4.5-6 and maximum at *pH* ~8 (no >8 values were tested). They ascribed this *pH*-dependence to structural changes in humic macromolecules, e.g., micelle formation at *pH* 4.5-6, a mechanism that might also be responsible for low CO dark production at low *pH*. The Q_{co}-*pH* relationships can be well described by a three-parameter exponential equation (Fig. 4-4).

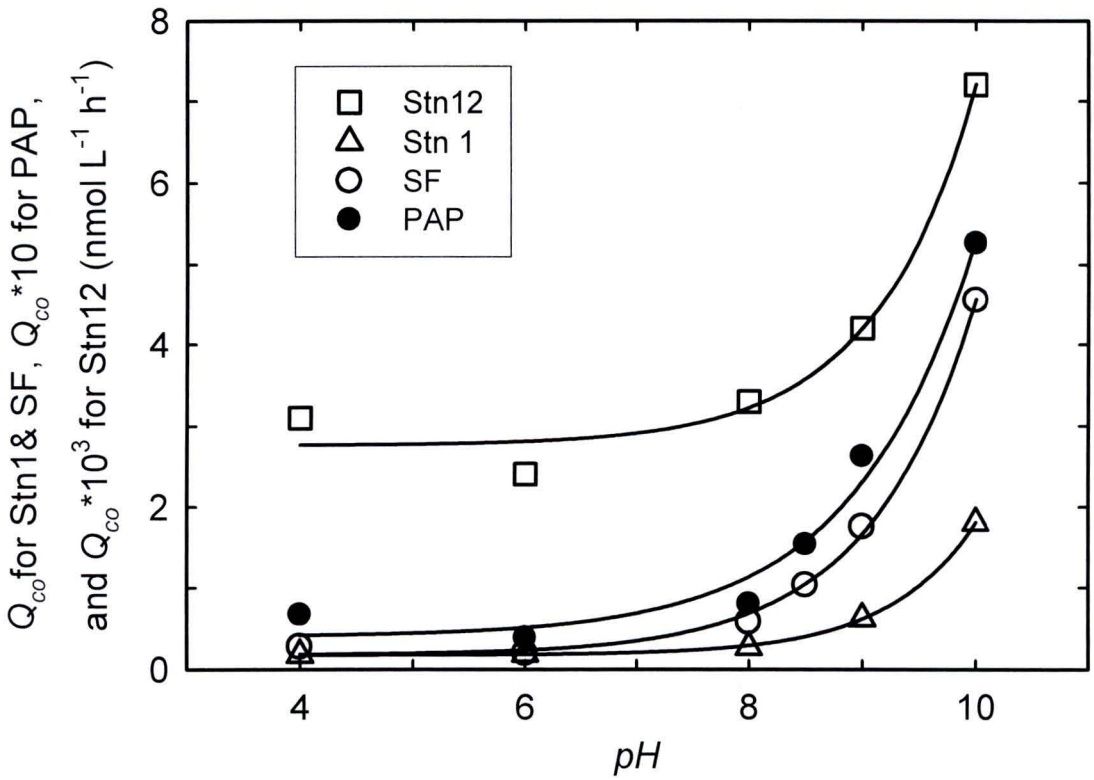

The best fit equation: $y = a + b \times \exp(c \times x)$

station	y	a	b	c	R^2
Stn 12	$Q_{co} \times 10^3$	2.76	5.72×10^{-5}	1.13	0.980
SF	Q_{co}	0.177	8.93×10^{-5}	1.08	0.998
Stn 1	Q_{co}	0.175	3.13×10^{-6}	1.32	1.00
PAP	$Q_{co} \times 10$	0.398	4.00×10^{-4}	0.95	0.982

Figure 4-4. Plots of Q_{co} vs. pH. Q_{co} was determined at 20°C. Lines are the best fits of the data.

4.3.4. Effects of sample storage, ionic strength, iron, and particles

Q_{co} in the PAP water decreased with storage time according to Q_{co} = 0.051 + 0.044 exp(-0.10 t) (R^2 = 0.996, n = 5), where t is storage time in days. If this equation also applies to other samples, Q_{co} from land-based incubations would be underestimated by 24-40% (average: 36%). The negative storage effect suggests that light and/or particles are involved in the production of CO precursors since our samples were 0.2-μm filtered and stored in the dark.

At ionic strengths (I) of 0.0, 0.2, 0.4, 0.6 and 1.0 mol L^{-1}, Q_{co} (mean ± SD, n = 4) in the RR sample was 0.43 ± 0.0077, 0.39 ± 0.0055, 0.42 ± 0.042, 0.40 ± 0.0059, and 0.41 ± 0.035 nmol L^{-1} h^{-1}, respectively. Ionic strength therefore did not significantly affect CO dark production, in contrast to the inverse relationship between I and CO photoproduction observed by Minor et al. (2006). Conformational changes of DOM and/or alteration in iron photochemistry, which are postulated to cause the effect of ionic strength on CO photoproduction (Minor et al., 2006), did not seem to influence the CO dark production.

Q_{co} in the DFOM-added RR sample did not appreciably differ from that in the original RR sample (9% higher in the DFOM treatment), indicative of no influence of Fe (Zepp et al.) on the CO dark production process. Again, this starkly contrasts the strong promotion of CO photoproduction by iron observed in the Rimouski River (Lou and Xie, 2006) and in some organic-rich rivers in the southeastern United States (Gao and Zepp, 1998; Xie et al., 2004).

An effort was made to evaluate the contribution of particles to abiotic, thermal CO production by poisoning whole water samples from Stn. PAP. We tested three widely used poisons, potassium cyanide (KCN), mercury chloride ($HgCl_2$), and sodium azide (NaN_3), and found they all gave rise to artifacts. KCN and $HgCl_2$ inhibited CO production while NaN_3 promoted it. The inhibition or promotion aggravated nonlinearly with increasing concentrations of the poisons. The concentration ranges tested were, KCN: 2.0-30.0 mg L^{-1}, $HgCl_2$ (saturated solution): 0.2-0.6 mL L^{-1}, and NaN_3: 0.2-0.5 g L^{-1}. A comparison was made between poisoned (2.0 mg L^{-1} KCN) whole water and poisoned (2 mg L^{-1} KCN), 0.2 μm-filtered water. Q_{co} in the filtered water was ~30% lower than in the whole water. Assuming that poisoning affected CO productions by particles and dissolved materials equally, we then may have underestimated the dark production in non-poisoned whole water samples by similar extent.

4.3.5 Multiple linear regression analysis

Taking into account the *S*, *T*, and *pH* dependences, we derived the following equation for predicting the CDOM-normalized CO dark production rate, β_{co}:

$$\ln(\beta_{co} \times 10^3) = -12305\ T^{-1} + 0.494\ pH - 0.0257\ S + 41.9 \qquad (4\text{-}1)$$

where β_{co} is in nmol L^{-1} h^{-1} m, and *T* in Kelvin. The *pH* data used for fitting the equation are in the range 6.0-9.0. If a_{350} is known, Q_{co} can be calculated as $\beta_{co} \times a_{350}$. Statistically, *T*, *S* and *pH* can explain 92.8% of the variance of Q_{co} (Fig. 4-5). The unaccounted variance could largely originate from varying sample storage times (Table 4-1). The

validity of Eq. 4-1 was checked by predicting the Q_{co} values for the SLES stations where in situ rates had been measured (Table 4-1). Compared to the in situ rates, the predicted rates are 31-49% lower at Stns. 1, 4 (both 2 and 50 m) and SF (2 m), 80% lower at Stn. SF (10 m), and 10% higher at Stn. SF (150 m). Therefore, the majority (4 out of 6) of the predicted values are ~40% lower, which is close to the 36% decrease in Q_{co} inferred from the sample storage test. To verify its applicability to blue waters, Eq. 4-1 was also validated with a sample from the Bermuda Atlantic Time-Series Study (BATS) site. The sample was collected at a depth of 40 m in late September, 2007 and had an in situ T: 26.7°C, S: 36.43, pH: 8.22, and a_{350}: 0.072 m^{-1}. It had been 0.2-μm-filtered and stored cold for 69 d before being incubated (27°C) for Q_{co} determination. The production rate was measured to be 0.0025 nmol L^{-1} h^{-1} while predicted to be 0.0039 nmol L^{-1} h^{-1}. Note that the storage time of the BATS sample was 50 d longer than the average storage time (19 d) of the samples used to derive Eq. 4-1. This difference would reduce the predicted Q_{co} to 0.0034 nmol L^{-1} h^{-1} if the Q_{co}-t relationshipfor the PAP sample (section 4.3.4) is applied. The measured value is hence 73% of the predicted value, a reasonably good match.

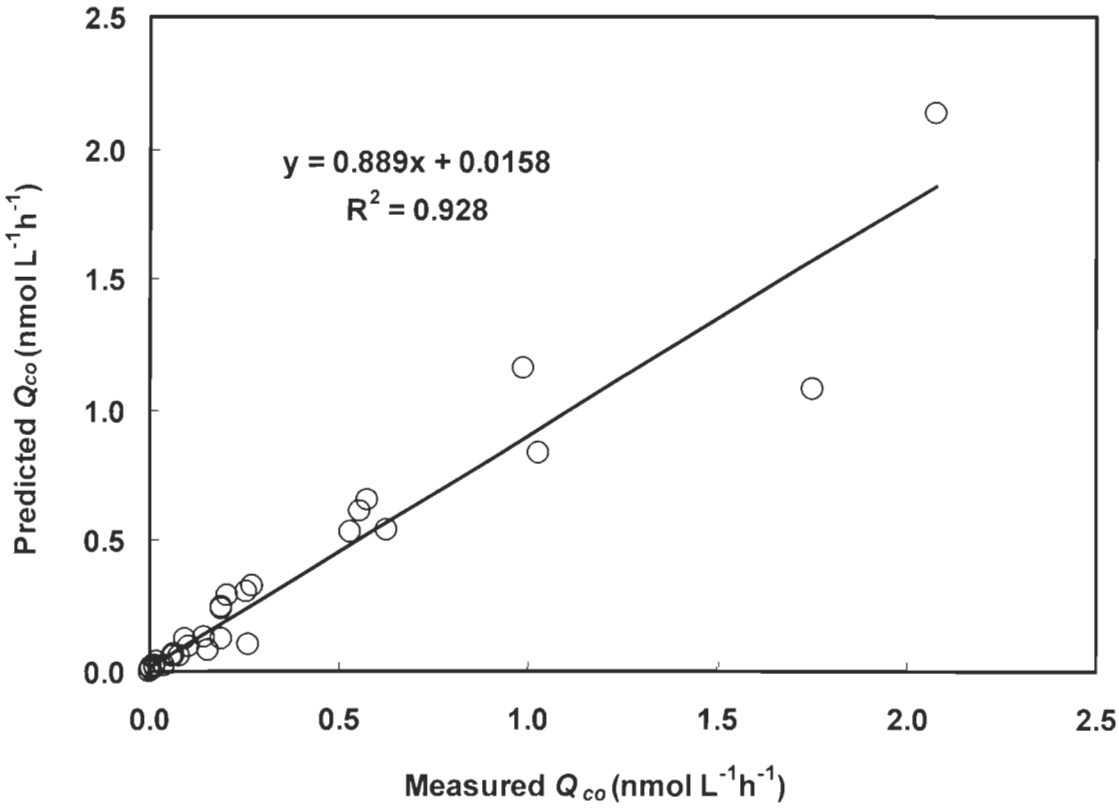

Fig.4-5. Q_{co} values predicted from Eq. 4-1 in the text vs. measured values. Line is the best fit of the data.

4.4. Fluxes of CO dark production in the SLES and global oceans

4.4.1. CO dark production in the SLES

Eq 4-1 was employed to estimate the seasonal and spatial distributions of the CO dark production flux in the SLES. The SLES is divided into the same sub-regions as for the assessment of CO photoproduction (see section 3.9.). The water columns of the LSLE and GSL are divided into the surface layer, cold intermediate layer (CIL), and bottom layer. The depth of the CIL is obtained from Smith et al. (2006a, 2006b). The water column of the USLE is regarded as only one layer since the USLE is fairly well mixed (Silverberg and El-Sabh, 1990). The water column of the Saguenay fjord is divided into the surface layer and the deep layer; the depth of surface layer was obtained from St-Onge and Hillaire-Marcel (2001). The temperature, salinity, pH and a_{350} data used to calculate Q_{co} were obtained from Petrie et al. (1996), Fortin and Pelletier (1995), and our St. Lawrence cruises in May 2007, July 2004, October 2005, and December 2005. Q_{co} values below 8.0×10^{-4} nmol L^{-1} h^{-1} are assumed negligible; this value is the upper limit predicted for the samples with undetectable CO dark production (Table 4-1).

Results are shown in Table 4-3. Note that both the sample storage and particle effects have been taken into account in these estimates under the assumption that the results from the PAP station are applicable to the entire SLES. Spatially, Q_{co} is the highest in the Saguenay Fjord and the ULSE, followed by the LSLE and the GSL (Table 4-3). Seasonally, Q_{co} is the highest in summer (1.91 Gg CO-C), followed sequentially by autumn (1.78 Gg CO-C), spring (0.28 Gg CO-C), and winter (0.20 Gg CO-C). The total flux is estimated as 4.2 Gg CO-C a^{-1}, with 98% from the surface layer and 2% from the

deeper layers, or 53% from GSL, 34% from the USLE, 5% from the LSLE, and 8% from the Saguenay Fjord.

The total CO production (e.g., dark plus photo) in the SLES is 29.1 Gg CO-C a^{-1}, with 86% from photoproduction and 14% from dark production, indicating that photoproduction is a dominate source. This CO production flux corresponds to 2.7% of the annual DOC discharge from the St. Lawrence River (1.13 Tg) reported by Hélie (2003) and 0.15% of the annual total primary production in the GSL and LSLE (19.77 Tg) modeled by Le Fouest et al. (2005). If CO is used as a proxy for photoproduction of dissolved inorganic carbon (DIC) at a ratio of 1 mol CO-C : 15 mol DIC (Miller and Zepp, 1995), the total remineralization rate by CO and DIC photoproduction and CO dark production amounts to 423.4 Gg C a^{-1}, which represents 37.4% of the DOC flux and 2.1% of the primary productivity.

Table 4-3. Annual CO dark production in the St. Lawrence Estuarine system.

Season	Region	Layer (m)	Area 10^4 km^2	T °C	S	pH	a_{350} m^{-1}	Q_{co}[b] nmol L^{-1} h^{-1}	CO[b] Gg C
Spring	Saguenay	Surface (0-15)	0.08	4.81	5.35	7.59	14.40	1.2E-01	0.04
		Bottom (15-250)	0.08	1.78	31.15	7.62	1.49	3.9E-03	0.02
	ULSE	Whole column (0-60)	0.35	4.79	9.75	7.76	3.63	2.9E-02	0.16
	LSLE	Surface (0-40)	0.94	1.02	28.34	7.80	1.07	2.9E-03	0.03
		CIL[a] (40-100)	0.94	0.31	31.85	7.80	0.45	/	/
		Bottom (100-300)	0.94	3.68	33.89	7.50	0.38	/	/
	GSL	Surface (0-40)	22.6	0.56	31.09	8.10	0.56	/	/
		CIL[a] (40-100)	22.6	0.00	32.10	8.00	0.45	/	/
		Bottom (100-300)	22.6	3.62	33.89	7.73	0.24	/	/
	Subtotal								0.25
Summer	Saguenay	Surface (0-10)	0.08	17.00	6.00	7.52	13.80	6.9E-01	0.15
		Bottom (10-250)	0.08	1.50	30.50	7.61	1.48	3.8E-03	0.02
	ULSE	Whole column (0-60)	0.35	12.00	9.55	7.70	4.20	1.0E-01	0.55
	LSLE	Surface (0-30)	0.94	5.15	28.49	7.78	1.50	7.9E-03	0.06
		CIL[a] (30-100)	0.94	0.93	31.89	7.79	0.44	/	/
		Bottom (100-300)	0.94	3.50	33.91	7.50	0.38	/	/
	GSL	Surface (0-30)	22.6	8.31	30.13	8.09	0.61	5.9E-03	1.06
		CIL[a] (30-100)	22.6	1.16	32.07	7.98	0.44	/	/
		Bottom (100-300)	22.6	3.64	33.91	7.75	0.22	/	/
	Subtotal								1.84

(to be continued)

Season	Region	Depth (m)	Area 10^4 km^2	T °C	S	pH	a_{350} m^{-1}	Q_{co}[b] nmol L^{-1} h^{-1}	CO[b] Gg CO-C
Autumn	Saguenay	Surface (0-15)	0.08	9.00	13.22	7.52	13.20	1.7E-01	0.05
		Bottom (15-250)	0.08	2.00	30.01	7.54	1.49	4.0E-03	0.02
	ULSE	Whole column (0-60)	0.35	8.00	9.72	7.72	4.80	6.2E-02	0.34
	LSLE	Surface (0-60)	0.94	3.57	29.43	7.59	0.95	3.5E-03	0.05
		CIL[a] (60-120)	0.94	1.62	32.14	7.53	0.45	/	/
		Bottom (120-300)	0.94	3.72	33.83	7.35	0.38	/	/
	GSL	Surface (0-60)	22.6	7.56	30.30	8.10	0.43	3.7E-03	1.32
		CIL[a] (60-120)	22.6	2.08	31.96	8.00	0.45	/	/
		Bottom (120-300)	22.6	3.64	33.83	7.75	0.24	/	/
	Subtotal								1.78
Winter	Saguenay	Surface (0-20)	0.08	0.00	13.02	7.50	13.00	3.9E-02	0.02
		Bottom (20-250)	0.08	1.50	30.00	7.52	1.40	3.5E-03	0.02
	ULSE	Whole column (0-60)	0.35	-0.30	9.68	7.73	4.62	1.6E-02	0.09
	LSLE	Surface (0-120)	0.94	0.13	30.23	7.78	0.99	2.2E-03	0.07
		Bottom (120-300)	0.94	3.91	33.94	7.45	0.37	/	/
	GSL	Surface (0-120)	22.6	0.65	31.21	8.07	0.41	/	/
		Bottom (120-300)	22.6	3.79	33.94	7.76	0.23	/	/
	Subtotal								0.19
	Grand total								4.06

[a]CIL stands for Cold Intermediate Layer;

[b]Effects of storage and particles have been taken into account.

4.4.2. CO dark production in global oceans

To estimate the global marine CO dark production flux, oceans are divided into coastal and blue waters along the 200-m isobath and are further divided into various latitudinal zones and two depth layers: the surface mixed layer (27.5°S-27.5°N: 0-50 m; >27.5°N (S): 0-100 m) and sub-surface layer (Tables 4-4 and 4-5). Area-weighted annual mean *T*, *S*, and zonal areas were derived from Levitus (1982). Blue-water *pH* is fixed at 8.1 and coastal water at 7.8. Salinity in coastal waters is set at 28.0. A modified version of the Sea*UV* algorithm (Fichot et al. 2008) was implemented on a ten-year (September 1997-August 2007) data set of SeaWiFS ocean color (monthly-binned at 9 km × 9 km) to derive $1^{\circ} \times 1^{\circ}$ monthly climatologies of surface-ocean (both blue and coastal waters) a_{350}. The published Sea*UV* algorithm was used to estimate the diffuse attenuation coefficient at 320 nm, Kd_{320}, from which a_{350} was computed by using a constant ratio $a_{320} \div Kd_{320} = 0.68$ and a CDOM spectral slope coefficient of -0.0194 nm^{-1}. The values for the ratio and spectral slope coefficient were derived from the data set used in the development of the Sea*UV* algorithm. The monthly climatologies were used to compute an annual average for each of the latitudinal zones shown in Tables 4-4 and 4-5. Open-ocean subsurface a_{350} data for the North Atlantic were from Nelson et al. (2007) and for the South Atlantic from Kitidis et al. (2006). Owing to lack of subsurface CDOM data in the Pacific and Indian Oceans, surface CDOM abundances were assumed to the subsurface layers there. This assumption is supported by limited available CDOM data from the equatorial Pacific (Simeon et al., 2003) and by relatively larger data sets from the Atlantic (Nelson et al., 1998; Nelson et al., 2007). CDOM in coastal waters was assumed to be vertically homogeneous.

Eq. 1 was then used to calculate Q_{co} for each zone and layer (with 50-m depth resolution). Zones and layers are omitted with $Q_{co} \leq 8.0 \times 10^{-4}$ nmol L^{-1} h^{-1}, which is the upper limit predicted for the SLES samples with undetectable CO dark production (Table 4-1). This treatment leads to negligible CO dark production in high northern and southern latitudes and at depths > 200 m except in the sub-tropical Indian Ocean (Table 4-4). The per-unit-volume rates are converted to the annual depth- and area-integrated CO dark production fluxes (Tables 4-4 and 4-5). Among the three main blue-water basins, the Pacific is the largest source (3.39 Tg CO-C a^{-1}), due mainly to its large size, while the source strengths in the Atlantic (1.34 Tg CO-C a^{-1}) and Indian Oceans (1.76 Tg CO-C a^{-1}) are similar. The global open-ocean production is thus 6.49 Tg CO-C a^{-1}, being 9.5 times the production in the global coastal waters (0.68 Tg CO-C a^{-1}). Vertically, dark production is slightly higher in the surface mixed layer (3.92 Tg CO-C a^{-1}) than in the deeper layer (3.27 Tg CO-C a^{-1}). The total dark source is estimated to be 7.19 Tg CO-C a^{-1}. Note that all these estimates do not account for the sample storage and particle effects as shown above. Applying the underestimations linked to sample storage (40%) and particles (30%) for the PAP water to global oceans, we arrive at a total dark source of 17.1 Tg CO-C a^{-1}, equivalent to 34% of the best available estimates of the global marine CO photoproduction flux (~50 Tg CO-C a^{-1}) (Zafiriou et al., 2003; Stubbins et al., 2006a). In the surface mixed layer, where most photoproduction occurs and where CO is available for exchange with the atmosphere, the dark production term is 9.33 Tg CO-C a^{-1} based on the storage- and particle-corrected dark source strengths. The mixed-layer dark source is therefore considerably larger than the best available estimates (3.7-5.52 Tg CO-C a^{-1}) of the global oceanic CO flux to the atmosphere (Bates et al., 1995; Stubbins et al.,

2006b). If dark and photo productions contribute to the CO flux proportionally according to their mixed-layer source strengths, 25% of the CO flux would arise from dark production. This percentage is slightly higher than the value (16.8%) of Kettle (2005) derived from modeling published CO profiles.

In deeper waters, dark production (7.78 Tg CO-C a^{-1}) should essentially be balanced by microbial consumption, which generally follows first-order kinetics at low [CO] (Xie et al., 2005). Knowing the first-order uptake rate constant, k_{bio}, would allow to estimate the deep steady-state [CO] (i.e., $Q_{co} \div k_{bio}$) or vice versa. Subsurface water (>100 m) k_{bio} data are rare. Jones (1991) determined k_{bio} from the surface to 900 m at a site in the Sargasso Sea. Unfortunately, the ^{14}C technique employed in that study could have substantially underestimated the obtained k_{bio} values (Xie et al., 2005). Using dark incubations of untreated whole samples collected in March at the BATS site, Kettle (1994) found no consistent depth-dependence of k_{bio} and acquired a k_{bio} of 0.026 h^{-1} at 200 m. This value is close to the rate constant (0.022 h^{-1}) recently reported by Zafiriou et al. (2008) for the upper 200-m layer in the same area and season. After correction for the storage and particle effects, Q_{co} at 200 m at BATS was estimated as 0.0026 nmol L^{-1} h^{-1} using T = 19°C (Zafiriou et al., 2008) and a_{350} = 0.060 m^{-1} (N.B. Nelson, unpublished data). The steady-state [CO] is thus 0.10 nmol L^{-1} based on Kettle's k_{bio} value. This predicted [CO] is within the BATS' 200-m [CO] range in March (0.02-0.12 nmol L^{-1}; mean: 0.05 ± 0.03 nmol L^{-1}) determined using improved CO sampling and analytical techniques (Zafiriou et al., 2008). In August 1999 at BATS, a k_{bio} of 0.028 h^{-1} in the 100-200 m layer was inferred from a limited number of deep CO profiles (Xie et al., unpublished data). Combining this rate constant with Q_{co} computed from the concurrently

measured 200-m T (~19°C) and a_{350} (0.033 m^{-1} (N.B. Nelson, unpublished data) gives a steady-state [CO] of 0.05 nmol L^{-1}. This value generally agrees with the measured August 200-m CO concentrations (range: 0.011-0.053 nmol L^{-1}; mean: 0.03 ± 0.01 nmol L^{-1}), which were comparable to the method's blank (Zafiriou et al., 2008). Hence, CO dark production, a potentially significant term in the global marine CO cycle, could be inadvertently ignored if judged only from its near blank-level concentrations at depth.

Potentially large uncertainties may exist in the current evaluation of global CO dark production since the empirical equation used to make the extrapolation was based on limited data obtained from an environment that is strongly influenced by terrestrial runoffs. Obviously, more blue water samples, in addition to the aforementioned BATS water, are needed to validate this equation. To improve the estimates, field measurements should be extended to other marine domains, particularly open oceans, to map CO dark production rates in diverse geographic regions; incubations should be carried out within the shortest time possible of sample collection to minimize sample storage effect; spatially and temporally denser sub-surface CDOM measurements are required if this term remains essential in future extrapolations. Efforts should also be made to characterize processes responsible for the production of CO precursors. For closure studies of deep-water CO cycling, simultaneous measurements are required of CO dark production rates, consumption rate constants and profiles (with improved methods). Finally, the role of particles in the CO dark production budget needs to be further elucidated.

Table 4-4. Annual CO dark production in blue waters (water depth >200 m).

Ocean	Region	Layer m	Area 10^4 km^2	T °C	Salinity	a_{350} m^{-1}	CO Tg C a^{-1}
Pacific	27.5-42.5°N	0-100	1507	14.77	34.0	0.096	0.15
	12.5-27.5°N	0-50	2263	24.33	34.8	0.044	0.20
		50-150	2263	20.28	34.8	0.044	0.23
	0-12.5°N	0-50	2921	27.02	34.4	0.068	0.59
		50-150	2921	20.26	34.7	0.068	0.45
	12.5°S-0	0-50	2620	26.44	35.2	0.067	0.47
		50-200	2620	21.52	35.4	0.067	0.70
	27.5-12.5°S	0-50	2299	23.24	35.6	0.046	0.18
		50-200	2299	20.23	35.6	0.046	0.35
	32.5-27.5°S	0-100	694	18.30	35.2	0.065	0.08
	Subtotal						3.39
Atlantic	27.5-42.5°N	0-100	925	17.83	35.9	0.080	0.11
	12.5-27.5°N	0-50	1215	24.62	36.5	0.055	0.13
		50-150	1215	21.35	36.7	0.052	0.16
	0-12.5°N	0-50	976	26.22	35.5	0.087	0.22
		50-150	976	18.21	35.9	0.096	0.15
	12.5°S-0	0-50	890	24.73	36.0	0.097	0.18
		50-150	890	17.85	35.8	0.074	0.10
	27.5-12.5°S	0-50	937	22.12	36.3	0.061	0.08
		50-150	937	18.78	36.0	0.064	0.11
	42.5-27.5°S	0-100	1056	14.88	35.1	0.091	0.10
	Subtotal						1.34
Indian	12.5-27.5°N	0-50	215	26.14	35.7	0.163	0.18
		50-600	212	17.38	35.9	0.163	0.28
	0-12.5°N	0-50	840	27.73	34.8	0.088	0.24
		50-200	840	19.80	35.2	0.088	0.23
	12.5°S-0	0-50	1300	27.16	34.6	0.061	0.24
		50-200	1300	19.03	35.0	0.061	0.22
	12.5-27.5°S	0-50	1287	23.82	35.2	0.051	0.12
		50-150	1287	20.52	35.4	0.051	0.15
	27.5-37.5°S	0-100	1038	16.93	35.5	0.079	0.11
	Subtotal						1.76
	Total						6.49

Table 4-5. Annual CO dark production in global coastal waters. (water depth <200m)。

Region	Layer	Area	T	a_{350}	CO
	m	10^4 km^2	°C	m^{-1}	Tg C a^{-1}
42.5-57.5°N	0-100	212.4	6.6	0.57	0.04
	100-200	39.3	5.4	0.57	0.006
27.5-42.5°N	0-100	108.4	16.0	0.46	0.06
	100-200	24.0	11.6	0.46	0.007
12.5-27.5°N	0-50	153.6	24.5	0.33	0.11
	50-200	43.8	19.9	0.33	0.05
0-12.5°N	0-50	198.0	27.0	0.29	0.17
	50-200	44.4	18.7	0.29	0.04
12.5°S-0	0-50	168.6	26.4	0.25	0.11
	50-200	26.8	20.0	0.25	0.02
27.5-12.5°S	0-50	61.2	23.2	0.23	0.02
	50-200	16.4	19.7	0.23	0.012
42.5-27.5°S	0-100	75.7	15.1	0.35	0.03
	100-200	12.7	12.5	0.35	0.003
52.5-42.5°S	0-100	42.6	6.0	0.37	0.004
	100-200	10.3	4.9	0.37	0.001
Total:					0.68

Chapitre 5. Conclusions

Cette thèse a pour la première fois quantifié les productions photochimique et abiotique non photochimiques de CO dans le système estuarien du St Laurent. Les distributions spatiales de Φ_{co} et de Qco et leurs rapports avec des paramètres hydrographiques ont été étudiés. Les implications sur le budget global du CO marin sont discutées. Les conclusions principales sont récapitulées comme suit :

(1) Le CDOM terrestre est plus efficace à produire photochimiquement du CO que le CDOM marin dérivé d'algues; et les groupements aromatiques sont probablement impliqués dans le processus photochimique. Le photoblanchiment du CDOM, principalement dans les premiers stades, a nettement diminué l'efficacité de la photoproduction de CO, Φ_{co}, pour les échantillons de faible salinité; mais le photoblanchiment n'a eu peu d'effet sur les échantillons les plus marins. Φ_{co} dépend modérément de la température de l'eau; pour une augmentation de 20°C, $\overline{\Phi}_{co}$ a augmenté de ~70% pour des échantillons de faible salinité et de 30-40% pour les échantillons salins.

(2) Le taux de production thermique, Qco, diminue horizontalement vers le large et verticalement vers le fond. Le CDOM s'est avéré un bon indicateur des précurseurs de CO pour la production thermique. Les substrats organiques terrestres ont semblé être plus

efficaces que leurs contre-parties marines en ce qui concerne la production thermique de CO. La dépendance en T de cette production aphotique de CO obéit à une équation d'Arrhénius avec une énergie d'activation pour l'eau douce considérablement plus haute que pour l'eau de mer. Le taux de production thermique est demeuré relativement stable entre pH 4-6, mais a augmenté constamment avec une augmentation supérieure du pH, un phénomène qui est fortement approprié au mélange d'estuaire. Contrairement à la photoproduction de CO, la force ionique et la présence de fer ont montrées peu d'influence sur la production thermique.

(3) La photoproduction annuelle de CO dans le SLES est estimée à 26.2 Gg CO-C, dont 89% est produit dans le GSL, avec la partie restante venant presqu'également de l'estuaire supérieur et inférieur du St Laurent, et du fjord de Saguenay. De façon saisonnière, l'été contribue pour 50%, le printemps 26%, l'automne 21% et l'hiver pour 3%. La production aphotique annuelle de CO dans le SLES est évaluée à 4.2 Gg CO-C, dont 53% provient du GSL, 34% de l'USLE, 5% du LSLE, et 8% du fjord de Saguenay. De façon saisonnière, la production thermique de CO est la plus haute en été (1.91 Gg CO-C), suivi séquentiellement par l'automne (1.78 Gg CO-C), le printemps (0.28 Gg CO-C) et l'hiver (0.20 Gg CO-C). On estime que le flux total de production photochimique et thermique de CO dans le SLES est de 30.4 Gg CO-C a-1, dont 86% est de source photochimique.

(4) On estime que le montant total de CO produit par des processus abiotiques non photochimiques dans l'océan global est de 17.1 Tg CO-C a-1, ce qui est significatif comparé à la meilleure évaluation disponible de la photoproduction océanique globale de CO de 50 Tg CO-C a-1. L'intensité de la source aphotique de CO dans la couche mélangée de surface (9.33 Tg CO-C A-1) peut à elle seule plus que contribuer à la meilleure évaluation actuelle du flux de CO vers l'atmosphère. Les concentrations de CO d'eau profonde en état stationnaire déterminées à partir de Qco et des taux de consommation microbiens de CO sont ≤0.1 nmol L-1.

Bibliography

Andrews, S. S.; S. Caron; O. C. Zafiriou. 2000. Photochemical oxygen consumption in marine waters: a major sink for colored dissolved organic matter? *Limnology and Oceanography 45*(2): 267-277.

Babin, M.; D. Stramski; G. M. Ferrari; H. Claustre; A. Bricaud; G. Obolensky; N. Hoepffner. 2003. Variations in the light absorption coefficients of phytoplankton, nonalgal particles, and dissolved organic matter in coastal waters around Europe. *Journal of Geophysical Research-Oceans 108*(C7): Doi 10.1029/2001jc000882.

Bates, T. S.; K. C. Kelly; J. E. Johnson; R. H. Gammon. 1995. Regional and seasonal-variations in the flux of oceanic carbon monoxide to the atmosphere. *Journal of Geophysical Research-Atmospheres 100*(D11): 23093-23101.

Bélanger, S.; M. Babin; P. Laroache. 2008. An empirical ocean color algorithm for estimating the contribution of chromophoric dissolved organic matter to total light absorption in optically complex waters. *J. Geophys. Res.*: doi:10.1029/2007JC004436, in press.

Bélanger, S.; H. X. Xie; N. Krotkov; P. Larouche; W. F. Vincent; M. Babin. 2006. Photomineralization of terrigenous dissolved organic matter in Arctic coastal waters from 1979 to 2003: Interannual variability and implications of climate change. *Global Biogeochemical Cycles 20*(4): doi:10.1029/2006gb002708.

Benner, R. 2002. Chemical composition and reactivity. In Biogeochemistry of marine dissolved organic matter. D. A. Hansell and C. A. Carlson. Eds, Academic Press London. pp: 59-90.

Buiteveld, H.; J. M. H. Hakvoort; M. Donze. 1994. The optical properties of pure water. SPIE proceedings on ocean optics XII. J. S. Jaffe. 2258: 174-183.

Canadian. ice service. 2001. Sea ice climatic atlas: east coast of Canada, 1971-2000. Ottawa, Canadian government publishing.

Conrad, R.; W. Seiler; G. Bunse; H. Giehl. 1982. Carbon monoxide in seawater (Atlantic Ocean). *J. Geophys. Res. 87*: 8839-8852.

d'Anglejan, B. 1990. Recent sediments and sediment transport processes in the St. Lawrence estuary. Oceanography of a large-scale estuarine system: the St. Lawrence. M. I. EI-SabhN. Silverberg, Springer-Verlag: 109-129.

d'Anglejan, B. F.; E. C. Smith. 1973. Distribution, transport and composition of suspended matter in the St. Lawrence Estuary. *Can. J. Earth Sci. 10*: 1380-1396.

Del Vecchio, R.; N. V. Blough. 2002. Photobleaching of chromophoric dissolved organic matter in natural waters: kinetics and modeling. *Mar. Chem. 78*: 231-253.

Derwent, R. G. 1995. Air chemistry and terrestrial gas emissions - a global perspective. *Philosophical Transactions of the Royal Society of London Series A-Mathematical Physical and Engineering Sciences 351*(Ser. A): 205-217.

Dickie, L.; R. W. Trites. 1983. The Gulf of St. Lawrence. Ecosystems of the world, 26: Estuaries and semi-enclosed seas. L. DickieR. W. Trites. Amsterdam, Elsevier Sci. Pub.: 403-425.

Doney, S. C.; R. G. Najjar; S. Stewart. 1995. Photochemistry, mixing and diurnal cycles in the upper ocean. *Journal of Marine Research 53*(3): 341-369.

Fichot, C. G.; S. Sathyendranath; W. L. Miller. 2008. SeaUV and SeaUVC: Algorithms for the retrieval of UV/Visible diffuse attenuation coefficients from ocean color. *Remote Sensing of Environment*: doi:10.1016/j.rse.2007.08.009.

Flock, O. R.; M. O. Andreae. 1996. Photochemical and non-photochemical formation and destruction of carbonyl sulfide and methyl mercaptan in ocean waters. *Marine Chemistry 54*: 11-26.

Fortin, G. R.; M. Pelletier. 1995. Synthèse des connaissances sur les aspects physiques et chimiques de l'eau et des sédiments du Saguenay. Zones d'intervention prioritaire 22 et 2. Environnement Canada, région du Québec, Conservation de l'environnement, Centre Saint-Laurent. Rapport technique: 212.

Gao, H. Z.; R. G. Zepp. 1998. Factors influencing photoreactions of dissolved organic matter in a coastal river of the southeastern United States. *Environmental Science & Technology 32*(19): 2940-2946.

Gearing, J. N.; R. Pocklington. 1990. Organic Geochemical studies in the St. Lawrence estuary. Oceanography of a large-scale estuarine system: the St. Lawrence. M. I. El-SabhN. Silverberg, Springer-Verlag.

Gnanadesikan, A. 1996. Modeling the diurnal cycle of carbon monoxide: sensitivity to physics, chemistry, biology, and optics. *Journal of Geophysical Research-Oceans 101*(C5): 12177-12191.

Gratton, Y.; G. Mertz; J. A. Gagné. 1988. Satellite observations of tidal upwelling and mixing in the St. Lawrence estuary. *J. Geophys. Res. 93*: 6947-6954.

Gueymard, C. 1995. SMARTS2, A simple model of the atmospheric radiative transfer of sunshine: algorithms and performance assessment. Professional paper FSEC-PF-270-95 Florida Solar Energy Center.

Gueymard, C. A. 2001. Parameterized transmittance model for direct beam and circumsolar spectral irradiance. *Solar Energy 71*(5): 325-346.

Hedges, J. I.; R. G. Keil; R. Benner. 1997. What happens to terrestrial organic matter in the ocean? *Organic Geochemistry 27*: 195-212.

Hélie, J.-F. 2003. Geochemistry and fluxes of organic and inorganic carbon in aquatic systems of eastern Canada: examples of the St. Lawrence River and the Robert–Bourassa reservoir- isotopic approach, Ph.D. thesis. Université du Québec à Montréal.

Hu, C. M.; F. E. Muller-Karger; R. G. Zepp. 2002. Absorbance, absorption coefficient, and apparent quantum yield: a comment on common ambiguity in the use of these optical concepts. *Limnology and Oceanography 47*(4): 1261-1267.

Hubbard, V. A.; A. Stubbins; K. Mopper. 2006. Evaluating CO photoproduction pathways from DOM using simple aromatics and lignin phenolics as model DOM choromophoric sites. *Eos Trans. AGU 2006, 87(36), Ocean Sci. Meet. Suppl., Abstract OS26Q-05.*

Johannessen, S. C.; W. L. Miller. 2001. Quantum yield for the photochemical production of dissolved inorganic carbon in seawater. *Marine Chemistry 76*(4): 271-283.

Johannessen, S. C. H. 2000. A photochemical sink for dissolved organic carbon in the ocean. Ph.D thesis. Dalhousie University (Canada), Halifax, Nova Scotia.

Johnson, J. E.; T. S. Bates. 1996. Sources and sinks of carbon monoxide in the mixed layer of the tropical South Pacific Ocean. *Global Biogeochemical Cycles 10*(2): 347-359.

Jones, R. D. 1991. Carbon-monoxide and methane distribution and consumption in the photic zone of the Sargasso Sea. *Deep-Sea Research Part I - Oceanographic Research Papers 38*(6): 625-635.

Kagan, J. 2003. Organic photochemistry, principles and applications, Chapter 4; Academic Press: San Diego, CA. pp. 55-64.

Kettle, A. J. 1994. A model of the temporal and spatial distribution of carbon monoxide in the mixed layer. Woods Hole, Mass., USA, Woods Hole Oceanogr. Inst.-Mass. Inst. of Technol. Joint program in Oceanogr.

Kettle, A. J. 2005. Diurnal cycling of carbon monoxide (CO) in the upper ocean near Bermuda. *Ocean Modelling 8*(4): 337-367.

Kieber, D. J.; J. Mcdaniel; K. Mopper. 1989. Photochemical source of biological substrates in seawater - implications for carbon cycling. *Nature 341*: 637-639.

Kieber, D. J.; B. H. Yocis; K. Mopper. 1997. Free-floating drifter for photochemical studies in the water column. *Limnology and Oceanography 42*(8): 1829-1833.

Kieber, R. J.; X. L. Zhou; K. Mopper. 1990. Formation of carbonyl compounds from UV-induced photodegradation of humic substances in natural waters - fate of riverine carbon in the Sea. *Limnology and Oceanography 35*(7): 1503-1515.

King, G. M. 2001. Aspects of carbon monoxide production and oxidation by marine macroalgae. *Marine Ecology-Progress Series 224*: 69-75.

Kitidis, V.; A. P. Stubbins; G. Uher; R. C. U. Goddard; C. S. Law; E. M. S. Woodward. 2006. Variability of chromophoric organic matter in surface waters of the Atlantic Ocean. *Deep-Sea Research Part II-Topical Studies in Oceanography 53*: 1666-1684.

Koutitonsky, V. G.; G. L. Bugden. 1991. The physical oceanography of the Gulf of St. Lawrence: a review with emphasis on the synoptic variability of the motion. The Gulf of St. Lawrence: small ocean or big estuary? J. C. Therriault, Can. Spec. Publ. Fish. Aquat. Sci.: 57-90.

Law, C. S.; T. N. Sjoberg; R. D. Ling. 2002. Atmospheric emission and cycling of carbon monoxide in the Scheldt Estuary. *Biogeochemistry 59*: 69-94.

Le Fouest, V.; B. Zakardjian; F. J. Saucier; M. Starr. 2005. Seasonal versus synoptic variability in planktonic production in a high-latitude marginal sea: The Gulf of St. Lawrence (Canada). *Journal of Geophysical Research-Oceans 110*(C9).

Levitus, S. 1982. Climatological atlas of the world ocean. Washington, D.C., National Oceanic and Atmospheric Administration, US Department of Commerce.

Lou, T.; H. X. Xie. 2006. Photochemical alteration of the molecular weight of dissolved organic matter. *Chemosphere 65*(11): 2333-2342.

Miller, W. L.; C. G. Fichot. 2006. Using remote sensing to calculate photochemical carbon oxidation in the coastal ocean. Eos Trans AGU 2006 87 (36), Ocean Sci. Meet. Suppl., Abstract OS24A-05.

Miller, W. L.; M. A. Moran. 1997. Interaction of photochemical and microbial processes in the degradation of refractory dissolved organic matter from a coastal marine environment. *Limnology and Oceanography 42*(6): 1317-1324.

Miller, W. L.; M. A. Moran; W. M. Sheldon; R. G. Zepp; S. Opsahl. 2002. Determination of apparent quantum yield spectra for the formation of biologically labile photoproducts. *Limnology and Oceanography 47*(2): 343-352.

Miller, W. L.; R. G. Zepp. 1995. Photochemical production of dissolved inorganic carbon from terrestrial organic matter - significance to the oceanic organic carbon cycle. *Geophysical Research Letters 22*(4): 417-420.

Minor, E. C.; J. Pothen; B. J. Dalzell; H. Abdulla; K. Mopper. 2006. Effects of salinity changes on the photodegradation and ultraviolet-visible absorbance of terrestrial dissolved organic matter. *Limnology and Oceanography 51*(5): 2181-2186.

Mopper, K.; J. Helms; A. Stubbins; N. Chen; E. Minor; B. Dalzell. 2006. Effect of pH and ionic strength on terrestrial DOM photoreactivity: implication in estuarine DOM transformations. *Eos Trans. AGU 2006, 87(36), Ocean Sci. Meet. Suppl., Abstract OS541-04.*

Mopper, K.; D. J. Kierber. 2000. Marine photochemistry and its impact on carbon cycling. The effects of UV radiation in the marine environment. S. de Mora et al. New York, Cambridge Univ. Press. 10: 101-129.

Moran, M. A.; W. L. Miller. 2007. Resourceful heterotrophs make the most of light in the coastal ocean. *Nature Reviews Microbiology 5*(10): 792-800.

Moran, M. A.; R. G. Zepp. 1997. Role of photoreactions in the formation of biologically labile compounds from dissolved organic matter. *Limnology and Oceanography 42*(6): 1307-1316.

Najjar, R. G.; D. J. Erickson; S. Madronich. 1995. Modeling the air-sea fluxes of gases formed from the decomposition of monoxide. The role of nonliving organic matter in the earth's carbon cycle: Report of the Dahlem workshop on the role of

nonliving organic matter in the earth's carbon cycle, Berlin,1993. R. G. Zepp and C. Sonntag. New York, Wiley: 107-132.

Nelson, N. B.; D. A. Siegel; C. A. Carlson; C. Swan; W. M. Smethie; S. Khatiwala. 2007. Hydrography of chromophoric dissolved organic matter in the North Atlantic. *Deep-Sea Research Part I-Oceanographic Research Papers 54*(5): 710-731.

Nelson, N. B.; D. A. Siegel; A. F. Michaels. 1998. Seasonal dynamics of colored dissolved material in the Sargasso Sea. *Deep-Sea Research Part I-Oceanographic Research Papers 45*(6): 931-957.

Nieke, B.; R. Reuter; R. Heuermann; H. Wang; M. Babin; J. C. Therriault. 1997. Light absorption and fluorescence properties of chromophoric dissolved organic matter (CDOM), in the St Lawrence estuary (Case 2 waters). *Continental Shelf Research 17*(3): 235-252.

Nuccio, J.; P. J. Seaton; R. J. Kieber. 1995. Biological production of formaldehyde in the marine-environment. *Limnology and Oceanography 40*(3): 521-527.

Perdue, E. M.; J. D. Ritchie. 2003. Treatise on geochemistry: surface and ground water, weathering, and soils. J. I. Drever, Elsevier-Pergamon: Oxford. 5: 273-318.

Petrie, B.; K. Drinkwater; A. Sandström; R. Pettipas; D. Gregory; D. Gilbert; P. Sekhon. 1996. Temperature, salinity and sigma-t atlas for the Gulf of St. Lawrence., Can. Tech. Rep. Hydrogr. Ocean Sci. 178.

Pope, R. M.; E. S. Fry. 1997. Absorption spectrum (380-700 nm) of pure water .2. Integrating cavity measurements. *Applied Optics 36*(33): 8710-8723.

Pos, W. H.; D. D. Riemer; R. G. Zika. 1998. Carbonyl sulfide (OCS) and carbon monoxide (CO) in natural waters: evidence of a coupled production pathway. *Marine Chemistry 62*: 89-101.

Prather, M.; D. Ehhalt; F. Denterner; R. G. Derwent; E. Dlugokenchy; E. Holland; I. Isaksen; J. Katima; V. Kirchhoff; P. Matson; P. Midgley; M. Wang. 2001. Atmospheric chemistry and greenhouse gases. climate change 2001: The scientific basis. contribution of working group 1 to the third assessment report of the intergovernmental panel on climate change. J. T. Houghton et al. Cambridge, Cambridge University Press: 239-287.

Redden, G. D. 1982. Characteristics of photochemical production of carbon monoxide in seawater. Corvallis, Oreg., Oregon State Univ. M.S.

Schafer, C. T.; J. N. Smith; R. Côté. 1990. The Saguenay Fjord: a major tributary to the St. Lawrence estuary. oceanography of a large-scale estuarine system: the St. Lawrence. M. I. El-SabhN. Silverberg, Springer-Verlag: 378-420.

Siegel, D. A.; S. Maritorena; N. B. Nelson; D. A. Hansell; M. Lorenzi-Kayser. 2002. Global distribution and dynamics of colored dissolved and detrital organic materials. *Journal of Geophysical Research-Oceans 107*(C12): doi: 10.1029/2001jc000965.

Silverberg, N.; M. I. El-Sabh. 1990. The St. Lawrence estuary: concluding remarks. Oceanography of a Large-Scale Estuarine System, The St. Lawrence. Coastal and Estuarine Studies. M. I. El-SabhN. Silverberg. New York, Springer~Verlag. 39: 421-429.

Simeon, J.; C. Roesler; W. S. Pegau; C. Dupouy. 2003. Sources of spatial variability in light absorbing components along an equatorial transect from 165 degrees E to 150 degrees W. *Journal of Geophysical Research-Oceans 108*(C10).

Smith, G. C.; F. J. Saucier; D. Straub. 2006a. Response of the lower St. Lawrence Estuary to external forcing in winter. *Journal of Physical Oceanography 36*(8): 1485-1501.

Smith, G. C.; F. J. Saucier; D. Straub. 2006b. Formation and circulation of the cold intermediate layer in the Gulf of Saint Lawrence. *Journal of Geophysical Research-Oceans 111*: C06011, Doi: 10.1029/2005jc003017.

St-Onge, G.; C. Hillaire-Marcel. 2001. Isotopic constraints of sedimentary inputs and organic carbon burial rates in the Saguenay Fjord, Quebec. *Marine Geology 176*: 1-22.

Strain, P.M. 1990. Oceanographie chimique dans le golfe du Saint-Laurent. Bull. Can. Sci. Halieut. Quat. 220. pp: 206.

Stubbins, A. 2001. Aspects of aquatic CO photoproduction from CDOM, University of Newcastle-upon-Tyne, U.K. Ph.D.: 201.

Stubbins, A.; G. Uher; C. S. Law; K. Mopper; C. Robinson; R. C. Upstill-Goddard. 2006a. Open-ocean carbon monoxide photoproduction. *Deep-Sea Research Part II-Topical Studies in Oceanography 53*: 1695-1705.

Stubbins, A.; G. Uhera; V. Kitidis; C. S. Law; R. C. Upstill-Goddard; E. M. S. Woodward. 2006b. The open-ocean source of atmospheric carbon monoxide. *Deep-Sea Research Part II-Topical Studies in Oceanography 53*(14-16): 1685-1694.

Swinnerton, J. W.; V. J. Linnenbom; R. A. Lamontagne. 1970. The ocean: a natural source of carbon monoxide. *Science 167*: 984-986.

Toole, D. A.; D. J. Kieber; R. P. Kiene; D. A. Siegel; N. B. Nelson. 2003. Photolysis and the dimethylsulfide (DMS) summer paradox in the Sargasso Sea. *Limnology and Oceanography 48*(3): 1088-1100.

Vahatalo, A. V.; M. Salkinoja-Salonen; P. Taalas; K. Salonen. 2000. Spectrum of the quantum yield for photochemical mineralization of dissolved organic carbon in a humic lake. *Limnology and Oceanography 45*(3): 664-676.

Vahatalo, A. V.; R. G. Wetzel. 2004. Photochemical and microbial decomposition of chromophoric dissolved organic matter during long (months-years) exposures. *Marine Chemistry 89*: 313-326.

Valentine, R. L.; R. G. Zepp. 1993. Formation of carbon-monoxide from the photodegradation of terrestrial dissolved organic-carbon in natural-waters. *Environmental Science & Technology 27*(2): 409-412.

Von Hobe, M.; G. A. Cutter; A. J. Kettle; M. O. Andreae. 2001. Dark production: a significant source of oceanic COS. *Journal of Geophysical Research-Oceans 106*(C12): 31217-31226.

Weishaar, J. L.; G. R. Aiken; B. A. Bergamaschi; M. S. Fram; R. Fujii; K. Mopper. 2003. Evaluation of specific ultraviolet absorbance as an indicator of the chemical composition and reactivity of dissolved organic carbon. *Environmental Science & Technology 37*(20): 4702-4708.

Xie, H.; O. C. Zafiriou. 2008. Light-induced production of carbon monoxide from particles in marine waters: Preliminary results. Oral presentation at the 2008 AGU Ocean Sciences Meeting, Orlando, Florida, March 2-7, 2008.

Xie, H. X.; S. S. Andrews; W. R. Martin; J. Miller; L. Ziolkowski; C. D. Taylor; O. C. Zafiriou. 2002. Validated methods for sampling monoxide and headspace analysis of carbon in seawater. *Marine Chemistry 77*(2-3): 93-108.

Xie, H. X.; M. Gosselin. 2005. Photoproduction of carbon monoxide in first-year sea ice in Franklin Bay, southeastern Beaufort Sea. *Geophysical Research Letters 32*(12): L12606, doi: 10.1029/2005GL022803.

Xie, H. X.; O. C. Zafiriou; W. J. Cai; R. G. Zepp; Y. C. Wang. 2004. Photooxidation and its effects on the carboxyl content of dissolved organic matter in two coastal rivers in the Southeastern United States. *Environmental Science & Technology 38*(15): 4113-4119.

Xie, H. X.; O. C. Zafiriou; T. P. Umile; D. J. Kieber. 2005. Biological consumption of carbon monoxide in Delaware Bay, NW Atlantic and Beaufort Sea. *Marine Ecology-Progress Series 290*: 1-14.

Yocis, B. H.; D. J. Kieber; K. Mopper. 2000. Photochemical production of hydrogen peroxide in Antarctic Waters. *Deep-Sea Research Part I-Oceanographic Research Papers 47*(6): 1077-1099.

Zafiriou, O. C.; S. S. Andrews; W. Wang. 2003. Concordant estimates of oceanic carbon monoxide source and sink processes in the Pacific yield a balanced global "blue-water" CO budget. *Global Biogeochemical Cycles 17*(1): 1015, Doi 10.1029/2001gb001638.

Zafiriou, O. C.; H. X. Xie; N. B. Nelson; R. G. Najjar; W. Wang. 2008. Diel carbon monoxide cycling in the upper Sargasso Sea near Bermuda at the onset of spring and in midsummer. *Limnology and Oceanography 53*(2): 835-850.

Zepp, R. G.; T. V. Callaghan; D. J. Erickson. 1998. Effects of enhanced solar ultraviolet radiation on biogeochemical cycles. *Journal of Photochemistry and Photobiology B-Biology 46*(1-3): 69-82.

Zepp, R. G.; D. J. Erickson III; N. D. Paul; B. Sulzberger. 2007. Interactive effects of solar UV radiation and climate change on biogeochemical cycling. *Photochemical & Photobiological Sciences 6*(3): 286-300.

Zhang, Y.; H. X. Xie; G. H. Chen. 2006. Factors affecting the efficiency of carbon monoxide photoproduction in the St. Lawrence estuarine system (Canada). *Environmental Science & Technology 40*(24): 7771-7777.

Ziolkowski, L. 2000. Marine photochemical production of carbon monoxide. Halifax, Nova Scotia, Canada, Dalhousie University (Canada): 121.

Zuo, Y.; R. D. Jones. 1995. Formation of carbon-monoxide by photolysis of dissolved marine organic material and its significance in the carbon cycling of the oceans. *Naturwissenschaften 82*(10): 472-474.

Appendix

Table A1. Spectral solar photon flux for calculating $\overline{\Phi}_{co}$.λ: nm; Q:photons s^{-1} cm^{-2} nm^{-1}

λ	Q	λ	Q	λ	Q	λ	Q	λ	Q	λ	Q
280	0.00E+00	334	8.38E+13	388	1.30E+14	442	2.65E+14	496	3.62E+14	550	3.93E+14
281	0.00E+00	335	8.36E+13	389	1.27E+14	443	2.87E+14	497	3.70E+14	551	3.85E+14
282	0.00E+00	336	8.47E+13	390	1.31E+14	444	2.88E+14	498	3.81E+14	552	3.94E+14
283	0.00E+00	337	8.34E+13	391	1.30E+14	445	3.09E+14	499	3.74E+14	553	3.95E+14
284	0.00E+00	338	8.81E+13	392	1.35E+14	446	3.16E+14	500	3.80E+14	554	3.93E+14
285	0.00E+00	339	8.58E+13	393	1.59E+14	447	3.15E+14	501	3.75E+14	555	3.96E+14
286	0.00E+00	340	7.73E+13	394	1.69E+14	448	3.22E+14	502	3.64E+14	556	3.92E+14
287	0.00E+00	341	8.22E+13	395	1.69E+14	449	3.05E+14	503	3.72E+14	557	3.95E+14
288	0.00E+00	342	9.07E+13	396	1.18E+14	450	3.19E+14	504	3.57E+14	558	4.01E+14
289	0.00E+00	343	9.63E+13	397	9.07E+13	451	3.36E+14	505	3.53E+14	559	3.99E+14
290	0.00E+00	344	9.81E+13	398	1.51E+14	452	3.34E+14	506	3.64E+14	560	3.92E+14
291	0.00E+00	345	9.49E+13	399	1.67E+14	453	3.42E+14	507	3.67E+14	561	3.89E+14
292	0.00E+00	346	1.00E+14	400	1.11E+14	454	3.59E+14	508	3.68E+14	562	3.82E+14
293	0.00E+00	347	9.08E+13	401	1.46E+14	455	3.52E+14	509	3.87E+14	563	3.79E+14
294	0.00E+00	348	8.63E+13	402	2.10E+14	456	3.30E+14	510	3.82E+14	564	3.94E+14
295	0.00E+00	349	9.60E+13	403	2.27E+14	457	3.33E+14	511	3.70E+14	565	3.89E+14
296	8.10E+08	350	9.67E+13	404	2.34E+14	458	3.41E+14	512	3.79E+14	566	3.93E+14
297	4.18E+09	351	9.43E+13	405	2.47E+14	459	3.44E+14	513	3.79E+14	567	3.94E+14
298	1.16E+10	352	9.51E+13	406	2.45E+14	460	3.56E+14	514	3.77E+14	568	3.94E+14
299	3.22E+10	353	1.00E+14	407	2.40E+14	461	3.55E+14	515	3.86E+14	569	3.84E+14
300	6.75E+10	354	1.10E+14	408	2.36E+14	462	3.46E+14	516	3.74E+14	570	3.93E+14
301	1.49E+11	355	1.04E+14	409	2.32E+14	463	3.47E+14	517	3.67E+14	571	3.93E+14
302	2.72E+11	356	1.02E+14	410	2.29E+14	464	3.55E+14	518	3.65E+14	572	3.86E+14
303	4.94E+11	357	1.16E+14	411	2.38E+14	465	3.63E+14	519	3.71E+14	573	3.89E+14
304	7.97E+11	358	1.22E+14	412	2.57E+14	466	3.66E+14	520	3.35E+14	574	3.78E+14
305	1.37E+12	359	1.16E+14	413	2.35E+14	467	3.59E+14	521	3.30E+14	575	3.90E+14
306	2.46E+12	360	1.02E+14	414	2.39E+14	468	3.48E+14	522	3.39E+14	576	4.00E+14
307	3.88E+12	361	9.08E+13	415	2.65E+14	469	3.56E+14	523	3.63E+14	577	4.01E+14
308	5.30E+12	362	8.63E+13	416	2.62E+14	470	3.45E+14	524	3.69E+14	578	3.95E+14
309	6.70E+12	363	1.16E+14	417	2.60E+14	471	3.53E+14	525	3.75E+14	579	3.90E+14
310	8.64E+12	364	1.10E+14	418	2.63E+14	472	3.56E+14	526	3.68E+14	580	3.94E+14
311	1.15E+13	365	1.05E+14	419	2.63E+14	473	3.50E+14	527	3.79E+14	581	3.95E+14
312	1.26E+13	366	1.18E+14	420	2.70E+14	474	3.43E+14	528	3.88E+14	582	3.86E+14
313	1.38E+13	367	1.19E+14	421	2.56E+14	475	3.63E+14	529	3.78E+14	583	3.96E+14
314	2.02E+13	368	1.23E+14	422	2.57E+14	476	3.66E+14	530	3.47E+14	584	4.00E+14
315	2.35E+13	369	1.43E+14	423	2.57E+14	477	3.60E+14	531	3.69E+14	585	4.03E+14
316	2.53E+13	370	1.45E+14	424	2.67E+14	478	3.70E+14	532	3.91E+14	586	4.07E+14
317	2.89E+13	371	1.39E+14	425	2.72E+14	479	3.66E+14	533	3.89E+14	587	4.07E+14
318	3.09E+13	372	1.37E+14	426	2.51E+14	480	3.62E+14	534	3.98E+14	588	4.05E+14
319	3.13E+13	373	1.48E+14	427	2.62E+14	481	3.77E+14	535	3.93E+14	589	3.97E+14
320	3.56E+13	374	1.39E+14	428	2.63E+14	482	3.73E+14	536	3.72E+14	590	4.04E+14
321	4.17E+13	375	1.39E+14	429	2.59E+14	483	3.79E+14	537	3.84E+14	591	4.01E+14
322	4.07E+13	376	1.26E+14	430	2.55E+14	484	3.75E+14	538	3.90E+14	592	3.69E+14
323	4.57E+13	377	1.12E+14	431	2.51E+14	485	3.83E+14	539	4.01E+14	593	3.64E+14
324	5.10E+13	378	1.14E+14	432	2.46E+14	486	3.76E+14	540	3.88E+14	594	3.91E+14
325	4.84E+13	379	1.31E+14	433	2.15E+14	487	3.70E+14	541	3.89E+14	595	3.92E+14
326	4.72E+13	380	1.37E+14	434	1.95E+14	488	3.66E+14	542	3.93E+14	596	3.96E+14
327	5.25E+13	381	1.61E+14	435	2.58E+14	489	3.20E+14	543	3.80E+14	597	3.96E+14
328	5.96E+13	382	1.60E+14	436	2.70E+14	490	3.23E+14	544	3.72E+14	598	3.91E+14
329	7.17E+13	383	1.38E+14	437	2.64E+14	491	3.53E+14	545	3.87E+14	599	3.95E+14
330	7.79E+13	384	1.52E+14	438	2.67E+14	492	3.54E+14	546	3.85E+14	600	3.98E+14
331	7.49E+13	385	1.30E+14	439	2.87E+14	493	3.74E+14	547	3.91E+14		
332	7.93E+13	386	9.77E+13	440	3.01E+14	494	3.73E+14	548	3.94E+14		
333	9.00E+13	387	9.73E+13	441	2.84E+14	495	3.56E+14	549	3.92E+14		

Table A2. The inputs for the SMARTS2 model.

Card #	Variables	Inputs	
1	Commets	Spring and Summer	Autumn and Winter
2	Site pressure	1013.25 mb	
3	Reference Atmosphere	Sub-Arctic Summer	Sub-Arctic Winter
4	Water vapor	Calculated from reference atmosphere and altitude	
5	Ozone	Use default from reference atmosphere	
6	Gaseous absorption	Pristine Atmosphere	
7	CO_2	370 ppmv	
7a	Extraterrestrial spectrum	Gueymard 2002 (synthetic)	
8	Aerosol model	S&F_Maritime	
9	Turbidity	Aerosol optical depth at 500nm: 0.085	
10	Albedo	Sea water	
10b	Tillt Albedo	Bypass	
11	Spectral range	280-800	
12	Output	280-800, 1 nm	
13	Circumsolar	Bypass	
14	Smoothing filter	Bypass	
15	Illuminance	Bypass	
16	UV	Bypass	
17	Solar Geometry	48.5°N, -68°W; Time zone: -5	

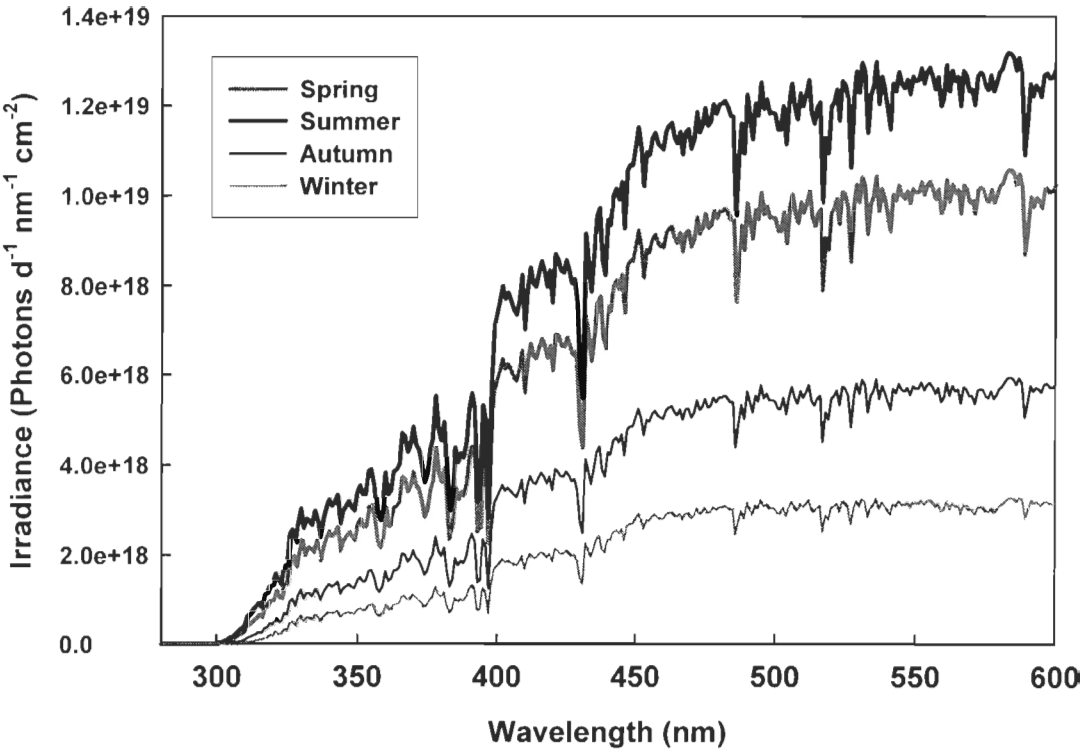

Figure A1. Seasonal spectral solar photon flux in the St. Lawrence Esturaine system